Research Square

Preprints are preliminary reports that have not undergone peer review.
They should not be considered conclusive, used to inform clinical practice,
or referenced by the media as validated information.

Catalytic and inhibitory architecture of comammox ammonia monooxygenase

Zongqiang Li

lizq6@sustech.edu.cn

Southern University of Science and Technology https://orcid.org/0009-0007-3833-6182

Tie-Qiang Mao

Southern University of Science and Technology

Xiaoyun Yang

Southern University of Science and Technology https://orcid.org/0000-0002-1374-2201

Zhi-Cong He

Shandong University

Jiawen Yang

Southern University of Science and Technology

Rihui Wu

Southern University of Science and Technology

Kenneth Leung

City University of Hong Kong https://orcid.org/0000-0002-2164-4281

Shengying Li

Institute of Marine Science and Technology, State Key Laboratory of Microbial Technology, Shandong University, Qingdao, China https://orcid.org/0000-0002-5244-870X

Ping Han

City University of Hong Kong https://orcid.org/0000-0001-6025-1651

Wei Peng

Shandong University https://orcid.org/0000-0002-4085-5842

Article

Keywords:

Posted Date: October 30th, 2026

DOI: https://doi.org/10.21203/rs.3.rs-11036410/v1

License: This work is licensed under a Creative Commons Attribution 4.0 International License.
Read Full License

Additional Declarations: There is **NO** Competing Interest.

Catalytic and inhibitory architecture of comammox ammonia monooxygenase

Authors: Tie-Qiang Mao[1]†, Xiaoyun Yang[1]†*, Zhi-Cong He[2]†, Jiawen Yang[1]†, Rihui Wu[1], Kenneth M.Y. Leung[3], Shengying Li[2], Ping Han[4,5]*, Wei Peng[2]* and Zongqiang Li[1]*

Affiliations:

[1]Department of Pharmacology, SUSTech Homeostatic Medicine Institute, School of Medicine, Institute for Biological Electron Microscopy, Southern University of Science and Technology, Shenzhen 518055, China.

[2]State Key Laboratory of Microbial Technology, Shandong University, Qingdao 266237, China.

[3]Department of Chemistry and State Key Laboratory of Marine Environmental Health, City University of Hong Kong, Hong Kong SAR 999077, China.

[4]School of Energy and Environment and State Key Laboratory of Marine Environmental Health, City University of Hong Kong, Hong Kong SAR 999077, China.

[5]Innovation Centre of Sustainability Energy and Environment, City University of Hong Kong Shenzhen Research Institute, Shenzhen 518057, China.

†These authors contributed equally to this work.

*Corresponding author. Email: lizq6@sustech.edu.cn

weipeng@sdu.edu.cn

pinghan@cityu.edu.hk

xiaoyun_y90@163.com

Abstract

Complete ammonia oxidizers (comammox) are widespread nitrifiers that can dominate ammonia oxidation in diverse environments by efficiently converting ammonia to nitrate within a single cell, yet the molecular basis distinguishing their ammonia monooxygenase (AMO) from those of canonical bacterial AMO remains unresolved. Here we report cryo-electron microscopy (cryo-EM) structures of AMO from the comammox *Nitrospira inopinata* (*Ni*AMO) in inhibitor-free and allylthiourea (ATU)-bound states at 2.47 Å and 2.68 Å resolution, respectively. *Ni*AMO displays distinctive auxiliary-subunit organization, copper-site configuration and hydrophobic-channel architecture. Integrative molecular dynamics (MD) and quantum mechanics/molecular mechanics (QM/MM) calculations support a methyl-plastoquinol (methyl-PQH_2)-coupled, Cu_D-centric catalytic model, with Cu_C potentially facilitating quinone redox cycling. *N. inopinata* exhibited broad susceptibility to several known nitrification inhibitors, and ATU-bound *Ni*AMO structure localized the inhibitor to the Cu_C–Cu_D region, accompanied by constriction of the hydrophobic channel, which is consistent with the competitive role of ATU demonstrated in recovery assays. Multi-omics analyses further revealed an energy-limited stress response to ATU, including induction of urea transport and utilization systems. Collectively, these findings define a methyl-PQ-linked catalytic and inhibitor-responsive architecture of comammox AMO and establish a mechanistic framework for lineage-aware management of nitrification in natural and engineered ecosystems.

Introduction

Nitrification is a cornerstone process in global nitrogen cycle and governs primary productivity, nitrogen retention and climate-relevant emissions[1,2]. Ammonia oxidation, the first and rate-limiting step of nitrification, is catalyzed by the integral membrane-bound ammonia monooxygenase (AMO), which converts NH_3 to hydroxylamine. AMO provides the primary energy-conserving reaction for ammonia-oxidizing archaea (AOA), ammonia-oxidizing bacteria (AOB) and complete ammonia oxidizers (comammox)[1,3-6]. AOA and AOB convert ammonia to nitrite, whereas nitrite-oxidizing bacteria (NOB) subsequently oxidize nitrite to nitrate[7].The discovery of comammox *Nitrospira*, which oxidize ammonia to nitrate within a single cell, overturns this long-standing division of nitrification between ammonia and nitrite oxidizers[3,6]. Comammox are now recognized across soils, freshwaters, sediments and engineered systems[8-11]. Their ecological reach extends to coastal Antarctica, where clade B comammox were abundant and actively incorporated $^{13}CO_2$ during nitrification at low temperature[12]. The cultured clade A species *N. inopinata* also has exceptionally high ammonia affinity[13] and can grow on guanidine as its sole source of energy, reductant and nitrogen; soil microcosms further suggest that guanidine-derived nitrogen can enter nitrification in agricultural systems[14]. These observations place comammox at the intersection of natural nitrogen cycling, extreme-environment microbiology and managed nitrogen inputs.

As an integral copper-dependent metalloenzyme, copper-site configuration and catalytic mechanism of AMO have long been central topics of investigation. Recent

AOB AMO structures have begun to reveal lineage-dependent subunit composition and copper coordination, where the simultaneously occupied Cu_C–Cu_D has been proposed to act concertedly with the reduced coenzyme Q ($CoQ10H_2$) as the physiological electron donor, while a conformational rearrangement of TM5 in the AmoC subunit enlarges the hydrophobic substrate channel[15-18]. Whether comammox AMO shares these structural features or instead couples a distinct active-site organization and reductant coupling to reactive oxygen-species generation and ammonia oxidation remains unresolved.

Beyond its biogeochemical significance, ammonia oxidation contributes to nitrous oxide (N_2O) production[19-22] and accelerates the conversion of fertilizer ammonium to mobile nitrate, promoting nitrogen loss, water contamination and eutrophication[23-26]. To address these issues, nitrification inhibitors (NIs), including nitrapyrin (2-chloro-6-(trichloromethyl)pyridine, NP), dicyandiamide (DCD), amidinothiourea (ASU), 3,4-dimethylpyrazole phosphate (DMPP), and allylthiourea (ATU), are therefore used to inhibit AMO activity[27-29]. Their efficacy varies with soil properties and ammonia-oxidizer composition, and some compounds affect non-target organisms[27,30,31]. Comammox and canonical AOB can respond differently to the same inhibitor, while comammox responses also vary among soils[32,33]. Since comammox contribute to nitrification in agricultural systems and can access alternative nitrogen substrates such as guanidine[14,34], inhibitors developed primarily around canonical AOB may not predictably control comammox activity. The molecular basis of this lineage-dependent inhibition remains unresolved because no inhibitor-bound structure of

comammox AMO has been available.

Here, we report cryo-EM structures of the *Ni*AMO, captured in inhibitor-free and inhibitor-bound states. These structures reveal distinct structural and mechanistic features of its auxiliary subunit composition, regulation of the substrate access channel, and the functional specialization between the Cu_C and Cu_D active sites. Structural and computational analyses support an inclined mononuclear Cu_D active site that exhibits elevated catalytic energy barrier with a species-specific reductant methyl-PQH_2, consistent with the lower catalytic activity of *Ni*AMO relative to AOB AMOs. Inhibition assays show that *N. inopinata* has the greatest susceptibility to most tested inhibitors among the three representative nitrifiers examined. Rescue assays suggest that ATU inhibits *Ni*AMO via substrate-competitive chelation of its intracellular copper centers. The ATU-bound structure directly visualizes a multilayered inhibitory mechanism involving copper chelation, channel closure and impaired reductant access. Multi-omics profiling further links direct ATU-mediated *Ni*AMO inhibition to an energy-limited cellular response and increased urea-acquisition capacity. Together, these findings link structural divergence, methyl-PQH_2-coupled redox chemistry and inhibitor sensitivity in comammox AMO, providing a molecular framework for lineage-aware interpretation and management of nitrifiers.

Results

Structure of *N. inopinata* AMO

To determine the structure of comammox AMO, we cultivated *N. inopinata* and

prepared an AMO-enriched membrane fraction (Supplementary Fig. 1). Subsequent cryo-EM single-particle analysis yielded a high-resolution reconstruction at a nominal resolution of 2.47 Å (Supplementary Fig. 2). Similar to previously characterized bacterial AMOs and pMMOs[15-17], *Ni*AMO forms a trimeric assembly in which each protomer comprises the canonical subunits AmoA, AmoB and AmoC, along with a newly identified transmembrane helix (hereafter Helix1) (Fig. 1a, b and Supplementary Fig. 3a-d). In contrast to the auxiliary helices observed in bacterial AMOs and pMMOs, Helix1 resolved in *Ni*AMO occupies a distinct structural position that enables intimate association with both AmoA and AmoC through tightly bound lipid molecules, and adopts a tilted orientation of approximately 55° relative to the membrane-embedded equatorial plane (Fig. 1b and Supplementary Fig. 4). By integrating the cryo-EM density, mass spectrometric data and genomic annotation from *N. inopinata*[3,6], we proposed the Helix1 as a structural fragment derived from the putative AmoD subunit or a downstream enzyme—such as nitrite oxidoreductase (NXR) (Supplementary Fig. 3c-e). Unexpectedly, three rod-like electron densities were found in the periplasmic cupredoxin domains of *Ni*AMO. These elongated densities are buried within a pocket at the base of the β-barrel formed predominantly by bulky side-chain (Fig. 1c, d and Supplementary Fig. 3f); their chemical identity and functional significance remain unknown.

The high-resolution structure of *Ni*AMO enables unambiguous modeling of the Cu_B and Cu_C sites (Fig. 1e and Supplementary Fig. 3b, g-h). In contrast, the Cu_D site lacks well-defined electron density, attributable to the conformational flexibility of the TM5-

TM6 loop (Fig. 1e). Recent biochemical and structural evidence indicate that the Cu_D site may constitute the catalytically active center of pMMO[35,36] and a dicopper center comprising Cu_C and Cu_D is simultaneously present in AOB AMOs[15,17]. To quantify copper occupancy, we performed inductively coupled plasma (ICP) mass spectrometry analysis. The results showed that copper content in inhibitor-free *Ni*AMO is comparable to that in the inhibitor-bound state (Fig. 1f), in which three copper ions in per protomer of AMO supported by cryo-EM structure (*vide infra*), suggesting that the Cu_D site is occupied in *Ni*AMO. Owing to the conformational flexibility of the TM5-TM6 loop, the conserved Cu_D-coordinating E205 remains unresolved, whereas the three other conserved Cu_D-coordinating residues-H212, H198 and N194-are clearly resolved in TM5 and TM6 respectively (Fig. 1e, g), suggesting that the E205 is more susceptible to structural heterogeneity at the Cu_D site.

Consistent with the recently identified nonprotein density near Cu_C and Cu_D sites in bacterial AMO[15,17], a quinone-like density was observed in the vicinity of this Cu_C and the unresolved Cu_D sites (Fig. 1e). Recent biochemical assays demonstrated that reduced coenzyme Q may function as a physiologically relevant electron donor for AMO activity of AOB[17], whereas spectrometric and biosynthetic studies identified methyl-PQs in comammox *Nitrospira*[37,38]. The modeled reduced methyl-PQ (methyl-PQH_2) headgroup is oriented toward both Cu_C and Cu_D, suggesting an efficient short-range electron transfer to facilitate ammonia oxidation[39]. Together with the coenzyme Q-linked electron donation reported for AOB AMO, this observation suggests lineage-specific coupling between AMO and quinone chemistry.

The transmembrane (TM) helices surrounding Cu_C–Cu_D region also distinguish *Ni*AMO from the published AOB AMO structure. In canonical AOB AMO structures with co-occupied Cu_C and Cu_D sites, outward displacement and local kinking of TM5 from AmoC enlarge the hydrophobic channel[15,17]. By contrast, TM5 in *Ni*AMO adopts a slightly more inward orientation, resembling structures with a mononuclear copper center (Fig. 1h, i). The upper segment of TM6 instead rotates by 24°-32° toward the central pore, resulting in an enlarged entrance of the hydrophobic channel (Fig. 1h, i and Supplementary Fig. 5). These structural differences indicate that TM6, rather than TM5, serves as the primary regulatory element governing the Cu_D coordination and the hydrophobic channel geometry in *Ni*AMO. Both the upper segments of TM5 and TM6 are highly conserved across diverse bacterial lineages, including comammox (clades A and B), AOB and methane-oxidizing bacteria (MOB) (Fig. 1g), suggesting that lineage-specific use of a conserved helical module generates distinct channel states and copper-site configurations. When considered together with the quinone-like density adjacent to the Cu_C–Cu_D region, these structural observations raise the possibility that methyl-PQH_2 may influence not only local electron transfer but also the dynamic organization of the Cu_D site.

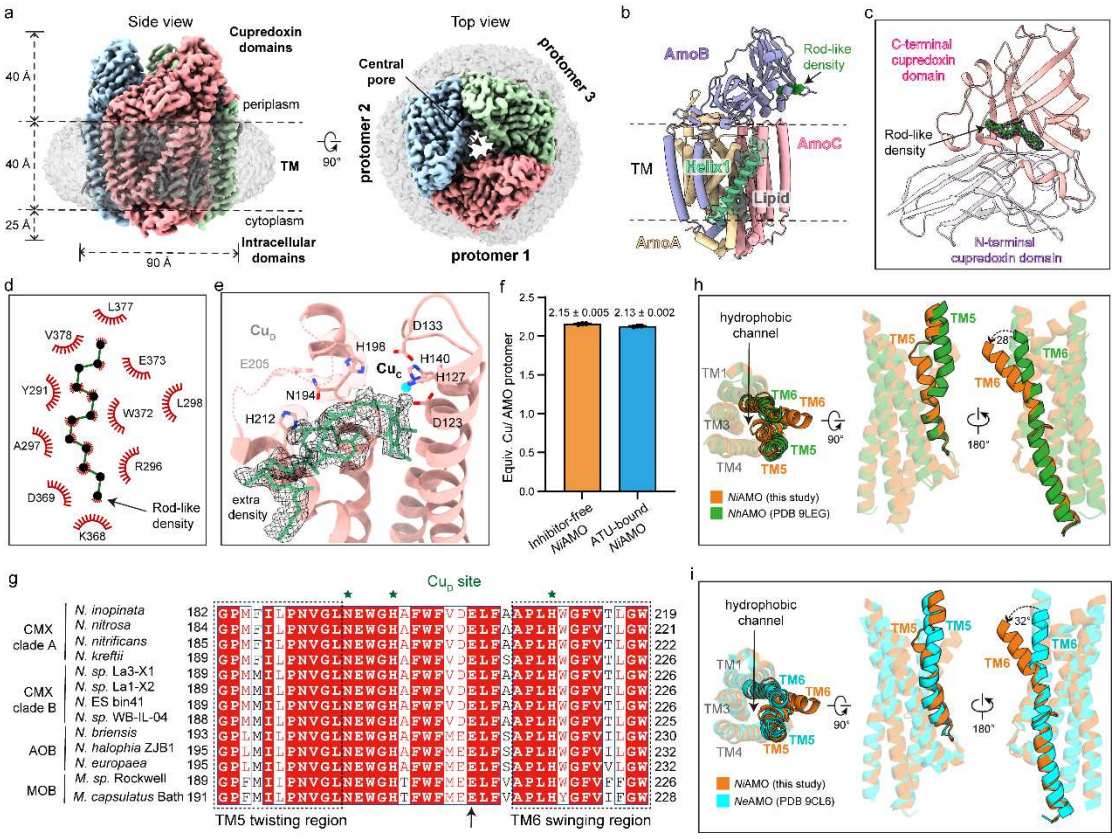


Fig. 1 | Overall structure of AMO from *N. inopinata.* **a,** Cryo-EM map of *Ni*AMO shown in two views. The three protomers are colored pink, blue and green; lipid densities are colored gray and the membrane bilayer is displayed as a transparent density. **b,** Model of one *Ni*AMO protomer, including AmoA (yellow), AmoB (purple), AmoC (pink), and Helix1 (green) with the corresponding density map. Lipid densities bridging Helix1 and the AMO core are depicted in gray. **c,** The rod-like density observed within the cupredoxin domains of AmoB. The N- and C-terminal cupredoxin domains are colored in purple and coral, and the unidentified density is shown in green. **d,** Close-up view showing the interactions between residues and the rod-like molecule. **e,** Coordination environments of Cu_C and Cu_D sites. An additional density is tentatively modelled as quinone-like molecule (green). The unresolved TM5-TM6 loop is depicted as dashed lines. **f**, Copper content of inhibitor-free *Ni*AMO and ATU-bound *Ni*AMO

189 from untreated and ATU-treated *N. inopinata* cells. Error bars represent standard
190 deviation of n = 3, each measured in triplicate. **g,** Sequence alignments from different
191 AOMs and MOBs demonstrate that the residues located within the twisting TM5 region,
192 TM6 swinging region and Cu_D coordinated residues are highly conserved. Red stars
193 represent the Cu_D coordinated residues. Black arrow indicates the conserved E205
194 residue. **h-i,** Structural comparisons of hydrophobic channels in *Ni*AMO (colored in
195 orange) with AOB AMOs containing co-occupied Cu_C–Cu_D center (**h**, PDB: 9LEG,
196 green) and a mononuclear copper center (**i**, PDB: 9CL6, cyan).
197
198 **Cu_D dynamics**
199 Despite the comparable copper content of inhibitor-free and inhibitor-bound *Ni*AMO
200 (Fig. 1f), the Cu_D site is poorly resolved in the inhibitor-free state. This lack of well-
201 defined density coincides with pronounced conformational flexibility of the TM5−TM6
202 loop surrounding the Cu_D region (Fig. 1e), raising the possibility that Cu_D is
203 dynamically coordinated rather than constitutively absent. To investigate whether the
204 presence of methyl-PQ influences Cu_D coordination, we performed long-timescale MD
205 simulations using inhibitor-free *Ni*AMO structure without (Supplementary Fig. 6) or
206 with methyl-PQH_2 (Supplementary Fig. 7). A free Cu ion was initially placed within the
207 Cu_D coordination environment and a plausible geometry was generated based on the
208 bacterial AMO model under distance and angle restraints[17]. The restraints were then
209 released to evaluate the intrinsic dynamics of Cu_D site.
210 In the methyl-PQH_2-free structure, interaction between Cu_D site and N194, H198 and

211 H212 progressively weakened and the Cu ion moved away from the coordination region
212 (Supplementary Fig. 6). By contrast, in the methyl-PQH_2-bound *Ni*AMO model, these
213 residues maintained a persistent coordination environment around the Cu ion
214 throughout the simulations (Supplementary Fig. 7). These observations support a
215 potential association between methyl-PQH_2 and enhanced stability of the Cu_D
216 coordination. However, compared with the Cu_C coordination, Cu_D exhibits substantially
217 greater conformational flexibility (Supplementary Figs. 6c and 7d), suggesting the
218 intrinsically dynamic nature of Cu_D site. Free-energy calculations further established a
219 direct energetic link between methyl-PQH_2 binding and stabilization of the Cu_D
220 coordination environment. In methyl-PQH_2-free *Ni*AMO, formation of the Cu_D-
221 coordinating state requires overcoming an energy barrier of 19.9 kcal/mol and is
222 strongly endergonic by 15.8 kcal/mol relative to the non-coordinating state
223 (Supplementary Fig. 8). By contrast, in methyl-PQH_2-bound *Ni*AMO, the
224 corresponding barrier is reduced to 7.7 kcal/mol, and the free-energy penalty of the
225 Cu_D-coordinating state decreases to 4.5 kcal/mol (Fig. 2a-d). These results indicate that
226 methyl-PQH_2 could facilitate the conformational reorganization required for Cu_D
227 coordination and stabilize the resulting coordination environment. Nevertheless, the
228 Cu_D-coordinating state remains moderately endergonic (4.5 kcal/mol) (Fig. 2c, d),
229 indicating that it is likely transiently or only partially populated rather than
230 constitutively occupied. Such dynamic and incomplete Cu_D occupancy precludes
231 unambiguous Cu_D density in the cryo-EM reconstruction, despite the preservation of
232 three of the four Cu_D-coordinating residues, consistent with the absence of Cu_D site in

the recently reported AOB AMO structure[16]. Collectively, these data indicate that Cu_D undergoes dynamic conformational change, and methyl-PQH_2 may facilitate transient assembly and stabilization of the Cu_D coordination environment.

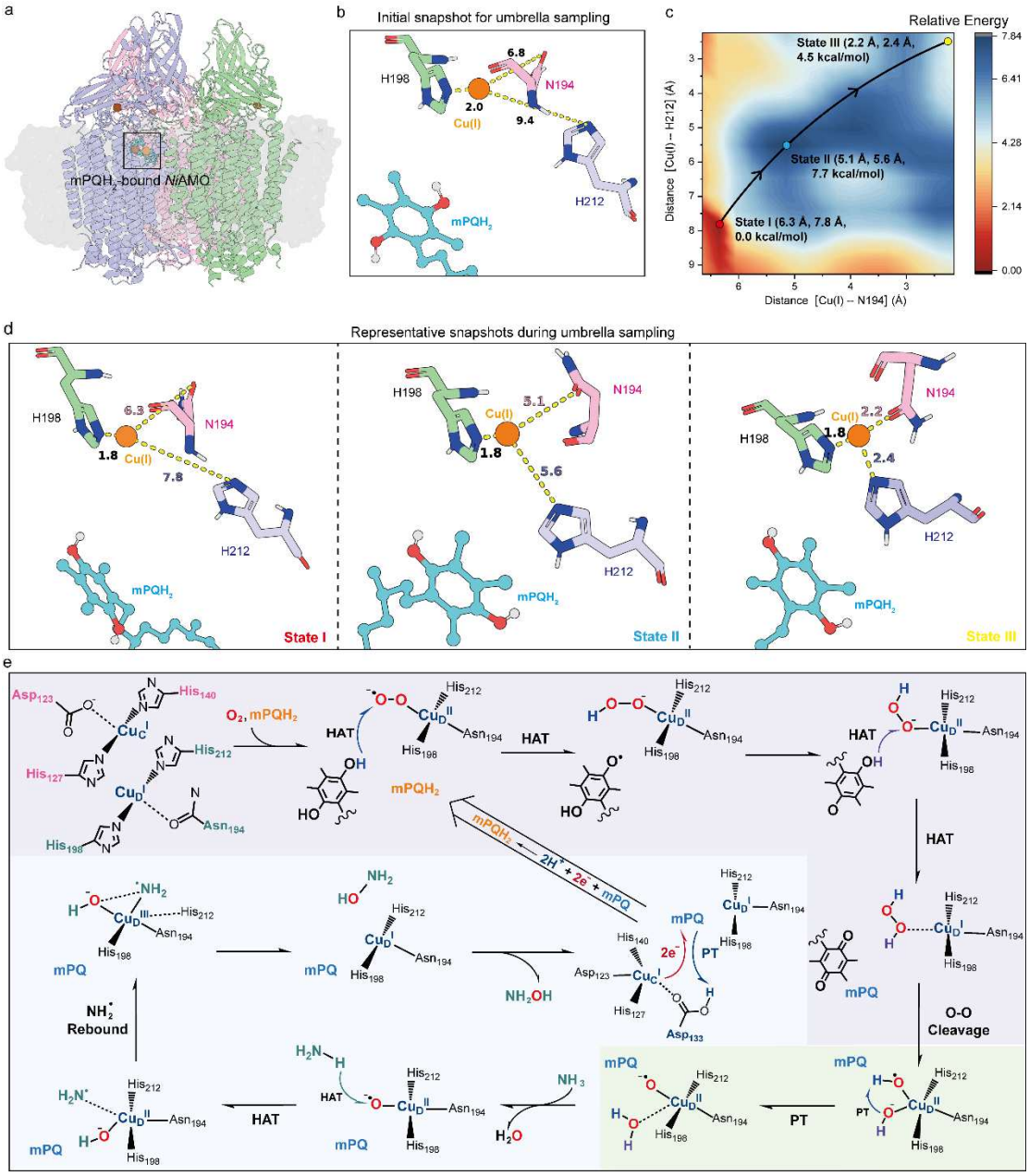


Figure 2 | Mechanistic insights into methyl-PQH_2-affected Cu_D binding and formation of the reactive copper-oxygen species. a, Overall structure of the membrane-bound *Ni*AMO-methyl-PQH_2 complex. The membrane is shown as a gray

surface. The Cu(I) ion of Cu_C site and methyl-PQH_2 resolved in the cryo-EM structure are colored as brown and cyan, respectively, whereas the Cu(I) ion randomly placed near the Cu_D site are shown as orange spheres. **b,** Initial snapshot for umbrella sampling (US) simulations, in which Cu(I) was placed near H198. N194, H198, and H212 are depicted as pink, green, and blue stick models, respectively. **c,** US-calculated the free energy profile (in kcal/mol) for the transition of Cu(I) from the initial non-coordinating state (State I) to the Cu-coordinating state (State III). The reaction coordinates were defined as the distances between Cu(I) and N194 and between Cu(I) and H212, respectively. **d,** Representative snapshots sampled along the transition pathway of Cu(I) from the uncoordinated to the coordinated state. Key distances are given in angstrom (Å). **e,** Overview of the proposed catalytic cycle mediated by the Cu_D active center. The reaction is initiated by O_2 activation at the Cu_D(I) site (purple background), followed by the formation of Cu_D-associated reactive oxygen species Cu_D(II)-$O^{\bullet-}$ generation (green background), substrate oxidation steps, ultimately leading to product formation (blue background).

Methyl-PQH_2-mediated formation of the reactive copper-oxygen species

To further probe the role of methyl-PQH_2 in *Ni*AMO catalysis, we simulated *Ni*AMO with methyl-PQH_2 and simultaneously occupied Cu_C and Cu_D sites. During the trajectories, the Cu_C–Cu_D distance progressively increased (~ 15 Å), whereas the quinol headgroup of methyl-PQH_2 preferentially approached the Cu_D center (~ 6 Å,

Supplementary Fig. 9). This geometry favors a catalytic configuration centered primarily at Cu_D, distinguishing *Ni*AMO from the more tightly coupled Cu_C–Cu_D model proposed for AMO of AOB[17] (two copper distance is ~ 8 Å [18]).

QM/MM and QM/MM metadynamics calculations were subsequently used to delineate how methyl-PQH_2 promotes O_2 activation and hydroxylation of NH_3 (Fig. 2e, Supplementary Tables 1-3). In the computed pathway, methyl-PQH_2 donates two hydrogen-atom equivalents sequentially to the $Cu_D(II)$–$O_2^{\bullet-}$ species, resulting in the formation of a $Cu_D(I)\cdots H_2O_2$ intermediate ($RC_{CuD} \rightarrow IC3_{CuD}$, Supplementary Fig. 10). Following the first hydrogen atom transfer (HAT), the resulting methyl-PQH radical undergoes a pronounced conformational reorganization before the second transfer takes place ($IC1_{CuD} \rightarrow IC2_{CuD}$, Supplementary Fig. 11). The highest computed electronic-energy barrier for conversion of $Cu_D(II)$–$O_2^{\bullet-}$ to $Cu_D(I)\cdots H_2O_2$ is 14.6 kcal/mol ($^3RC_{CuD} \rightarrow {}^3TS1_{CuD}$), and the *in situ* formation of H_2O_2 is exergonic by 19.8 kcal/mol ($^1IC3_{CuD}$). Notably, the initial HAT step mirrors that in AOB AMO, forming a $Cu_D(II)$–OOH^- intermediate. However, the subsequent reactivity of this intermediate depends on the distinct Cu_C–Cu_D geometry. In AOB AMO, the shorter Cu_C–Cu_D distance enables $Cu_D(II)$–OOH^- to interact with $Cu_C(II)$, yielding a bridging dicopper oxygen species (two copper distance is ~ 8 Å [18]). By contrast, the longer dicopper distance and greater steric constraint in *Ni*AMO prevent this bimetallic coupling, diverting the intermediate toward H_2O_2 formation and mononuclear Cu_D-mediated O–O bond cleavage (Fig. 2e). This mechanism echoes a previously proposed mode of reactive oxygen-species generation in pMMO, in which a quinol cofactor participates directly in assembling the

283 oxidizing species at a mononuclear copper center[39].

284 The newly formed H_2O_2 is directly recruited for the subsequent catalytic step. Electron
285 transfer (ET) from Cu_D(I) weakens and cleaves its O–O bond with a barrier of 17.5 kcal
286 mol^{-1}, producing Cu_D(II)–OH^- together with a hydroxyl radical (•OH) ($IC3'_{CuD} \rightarrow$
287 $IC4_{CuD}$, Supplementary Fig. 12). A subsequent HAT, accompanied by H_2O formation,
288 converts this transient radical pair into the reactive Cu_D(II)–$O^{\bullet-}$ species (Fig. 2e). Thus,
289 methyl-PQH_2 drives a confined process of O_2 reduction, H_2O_2 formation and O–O bond
290 cleavage that generates a copper–oxygen species capable of substrate oxidation. Once
291 formed, Cu_D(II)–$O^{\bullet-}$ activates an N–H bond of NH_3 and promotes the ensuing formation
292 of NH_2OH with an overall barrier of 17.2 kcal mol^{-1} (Fig. 2e and Supplementary Fig.
293 13). Collectively, the calculations support a Cu_D-centered pathway for oxygen-
294 activation and ammonia-hydroxylation.

295 The Cu_C site may instead facilitate local regeneration of the quinol reductant. In the
296 modeled reaction, oxidized methyl-PQ is first converted to the methyl-$PQH^{\bullet}$ radical
297 through a proton-transfer (PT)-triggered electron-transfer process, in which protonated
298 D133 supplies the proton while Cu_C(I) provides the electron. This first reduction step
299 proceeds with a barrier of only 1.2 kcal mol^{-1} (Fig. 2e and Supplementary Fig. 14). The
300 resulting methyl-$PQH^{\bullet}$ radical subsequently undergoes conformational reorientation,
301 positioning it for a second proton-coupled reduction that generates methyl-PQH_2 with
302 a barrier of 9.1 kcal mol^{-1} and an overall reaction free energy of −9.3 kcal mol^{-1}
303 (Supplementary Fig. 15). The calculations implicate D133, located adjacent to Cu_C, as
304 a plausible proton donor during this local redox process (Supplementary Fig. 16).

Notably, the intermediate Cu_C–D133 distance observed in the cryo-EM structure may be compatible with interconversion between a protonated, non-coordinating D133 state and a deprotonated, Cu-coordinating state (~ 3.3-3.5 Å, Supplementary Fig. 3h), providing a possible structural basis for coupling proton transfer to the local Cu_C redox chemistry.

Together, these data support a bipartite catalytic model in which Cu_D is proposed to serve as the primary site for O_2 activation and substrate hydroxylation, whereas Cu_C may mainly facilitate local methyl-PQ/methyl-PQH_2 redox cycling. Such functional partitioning provides a plausible framework for coupling spatially separated oxygen activation and reductant regeneration within *Ni*AMO. This model differs from a recently proposed concerted Cu_C–Cu_D catalytic model for AOB AMO [18] and raises the possibility of lineage-specific modes of copper-site utilization and quinone coupling.

Structure of *Ni*AMO-inhibitor complex

To assess whether structural differences among AMOs translate into differential inhibitor susceptibility, we measured the IC_{50} values of five representative NIs against pure cultures of *N. inopinata* (Comammox), *N. maritimus* SCM1 (AOA) and *N. halophila* ZJB1 (AOB) (Fig. 3a, b and Supplementary Fig. 17).

The three phylogenetically distinct lineages displayed divergent susceptibility profiles, with IC_{50} values spanning more than three orders of magnitude. *N. inopinata* was the most sensitive of the three isolates to ATU, DMPP, DCD and NP at sub- to low-micromolar concentrations. *N. halophila* ZJB1 was highly sensitive to two thiourea

derivatives ATU and ASU but comparatively resistant to DCD and NP. By contrast, *N. maritimus* SCM1 showed relatively low susceptibility to the inhibitors evaluated here (Fig. 3b and Supplementary Fig. 17), consistent with the previous observations[29]. Thus, *N. inopinata* showed the greatest inhibitor susceptibility among the three tested representatives. Its comparatively wider hydrophobic-channel opening, as revealed by structural analysis above, provides a mechanistic hypothesis for enhanced inhibitor access to the *Ni*AMO catalytic region.

Among the tested NIs, ATU showed the strongest inhibitory activity against *N. inopinata* (Fig. 3b). To elucidate the mechanistic basis of ATU-mediated inhibition, whole-cell assays were conducted (Fig. 3c, d). Exogenous $CuCl_2$ failed to restore ammonia oxidation inhibited by ATU (Fig. 3c), indicating that ATU targets the intracellular copper center of AMO rather than scavenging bioavailable copper ions. Under ATU treatment, urea hydrolysis remained active and urea-derived ammonia was rapidly consumed in untreated controls (Fig. 3d), showing that ATU does not directly impair urease activity. Urea hydrolysis can therefore increase ammonia supply during ATU exposure, but it does not bypass the requirement for *Ni*AMO in subsequent ammonia oxidation. Partial relief of inhibition was observed upon supplementation with either NH_4^+ or urea-derived ammonia (Fig. 3d), consistent with substrate competition. These data support a copper-chelating, substrate-competitive mode of ATU inhibition in *N. inopinata* that differs from the recently observed in AOA[40]. To further resolve the structural basis of ATU inhibition, *Ni*AMO was purified from ATU-treated *N. inopinata* cells, and its cryo-EM structure was determined at 2.68 Å

resolution (Fig. 3e and Supplementary Fig. 18). The overall structure of the *Ni*AMO-ATU complex closely resembles the inhibitor-free form (Fig. 3e, f and Supplementary Fig. 19a, b). A weak but discernible TM helix density adjacent to AmoC, hereafter Helix2, becomes visible in the inhibited state (Fig. 3f, Supplementary Figs. 4 and 19b). Helix2 comprises approximately 26 residues, lacks detectable periplasmic or cytoplasmic extensions, and packs against TM3, TM4 and TM5 of AmoC through lipid-mediated contacts (Fig. 3f). Its presence maybe reflect reduced conformational dynamics following ATU-induced inactivation.

In *Ni*AMO-ATU complex, no detectable ATU density was found in the Cu_B site (Supplementary Fig. 19c), supporting previous evidence that Cu_B site is not the catalytic center of AMO[15,17]. In contrast, a well-defined ATU-derived density was clearly resolved within the hydrophobic channel. ATU simultaneously chelated both Cu_C and Cu_D through its sulfur and nitrogen atoms, thereby stabilizing the Cu_D site into a defined conformation coordinated by N194, H198 and H212 (Fig. 3g and Supplementary Fig. 19d, e). ATU binding also enhanced the structural order of the TM5-TM6 loop. In this loop, E205 protrudes into the upper opening of the hydrophobic channel, where it forms a lid-like structure with F207, suggesting its potential role in regulating substrate access to the catalytic center (Fig. 3g, h and Supplementary Fig. 19e). Two newly formed hydrogen bonds from H212-F207 and N208-D51, further stabilize the conformation of this loop (Supplementary Fig. 19e).

Simultaneous chelation of Cu_C and Cu_D by ATU reduces the intermetallic distance to 4.8 Å and induces the conformational change in the surrounding helices that line the

hydrophobic channel (Fig. 3g, h). Compared with the active *Ni*AMO structure, the upper segment of TM5 undergoes a subtle outward shift, whereas the upper segment of TM6 dramatically rotates inward by ~37°, collectively reducing the hydrophobic channel volume (Fig. 3h). In addition, rearrangement of the Cu_C–Cu_D center abolishes quinone-like density (Fig. 1e), indicating that inhibitor binding and hydrophobic channel closure to block access of the endogenous reductant to the catalytic center.

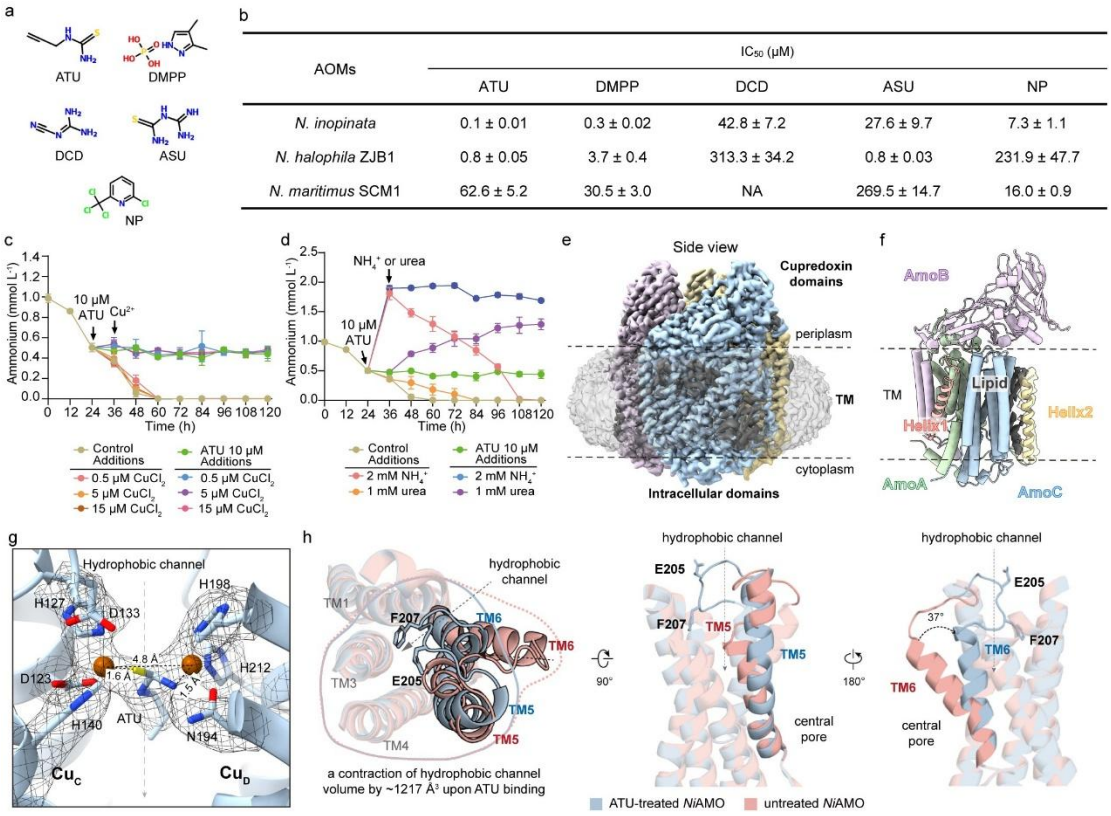


Fig. 3 | Overall structure of *Ni*AMO in complex with ATU. a, Chemical structures of five tested NIs. **b,** Differential inhibitory profile of NIs across phylogenetically distinct AOMs. IC_{50} values are expressed in micromolar (μM) and data are represented as mean ± SD (n = 3). NA: no inhibition detected at the tested concentration. **c-d,** Stress relief experiments on ATU-treated *N. inopinata* cells. Additions of copper **(c)** and ammonium and urea **(d)** to cultures treated with 10 μM ATU. Error bars represent

384 standard deviations of the mean (triplicates). Black arrows indicate the time of addition
385 of ATU, copper, ammonium, or urea to ATU-treated and control cultures. **e,** Cryo-EM
386 density map of ATU-treated *Ni*AMO shown in side view. **f,** Atomic model of ATU-
387 treated *Ni*AMO protomer, including AmoA (green), AmoB (light purple) and AmoC
388 (blue), together with Helix1 (coral) and the newly resolved Helix2 (yellow). Lipid
389 densities bridging Helix2 and the AMO core are depicted in gray. **g,** The simultaneous
390 presence of Cu_C and Cu_D sites within the hydrophobic channel of inhibitor-bound
391 *Ni*AMO. A well-defined ATU-derived density is positioned between Cu_C and Cu_D. **h,**
392 Structural comparison of hydrophobic channels between ATU-treated (blue) and
393 untreated *Ni*AMO (coral).
394
395 **Mechanism of ATU-mediated *Ni*AMO inhibition**
396 Structural comparison of inhibitor-free and ATU-bound *Ni*AMO revealed that the
397 conformational changes are concentrated around the Cu_C–Cu_D region and the upper
398 hydrophobic channel. In the inhibitor-free structure, the channel adopts an open
399 configuration and contains a quinone-like density near the copper sites. In the ATU-
400 bound structure, the inhibitor occupies the catalytic region, chelates both copper ions,
401 contracts the hydrophobic channel and blocks reductant accessibility (Figs. 1 and 3).
402 US simulations further showed that ATU could spontaneously access the *Ni*AMO,
403 traverse a substrate channel with a minimum diameter of 6.7 Å en route to the Cu_C site
404 (overcoming an energy barrier of 9.0 kcal/mol, Fig. 4a-c and Supplementary Fig. 20),
405 and trigger structural reorganization of the Cu_D coordination environment into an

ordered Cu_D-bound configuration (Fig. 4d, e and Supplementary Fig. 21). This transition proceeds with a low activation barrier of 6.7 kcal/mol and is thermodynamically favorable (−4.2 kcal/mol), indicating that ATU binding both kinetically facilitates and thermodynamically stabilizes Cu_D coordination. These computational results are consistent with the well-resolved Cu_D density observed in the ATU-bound *Ni*AMO structure (Fig. 3g and Supplementary Fig. 19e).

These observations support a coupled mechanism for ATU-mediated *Ni*AMO inhibition (Fig. 4f). First, ATU directly occupies the copper-containing cavity, preventing the catalytic region from adopting the dynamic configurations proposed for oxygen activation and substrate oxidation. Second, ATU-coupled rearrangements of TM5, TM6 and the TM5–TM6 loop promote formation of an E205/F207-containing lid and constrict the channel entrance, further restricting substrate access to the catalytic center. Third, the ATU-induced structural reorganization coincides with the loss of the quinone-like density, disrupting the local environment proposed to support electron and proton delivery.

ATU therefore inactivates *Ni*AMO through coordinated active-site occupation, channel closure and interference with electron and proton transfer. This multi-layered mechanism explains the high potency of ATU against *N. inopinata* and highlights the Cu_C–Cu_D region, TM5-TM6 gating module and associated reductant-binding environment as interdependent determinants of *Ni*AMO inhibition.

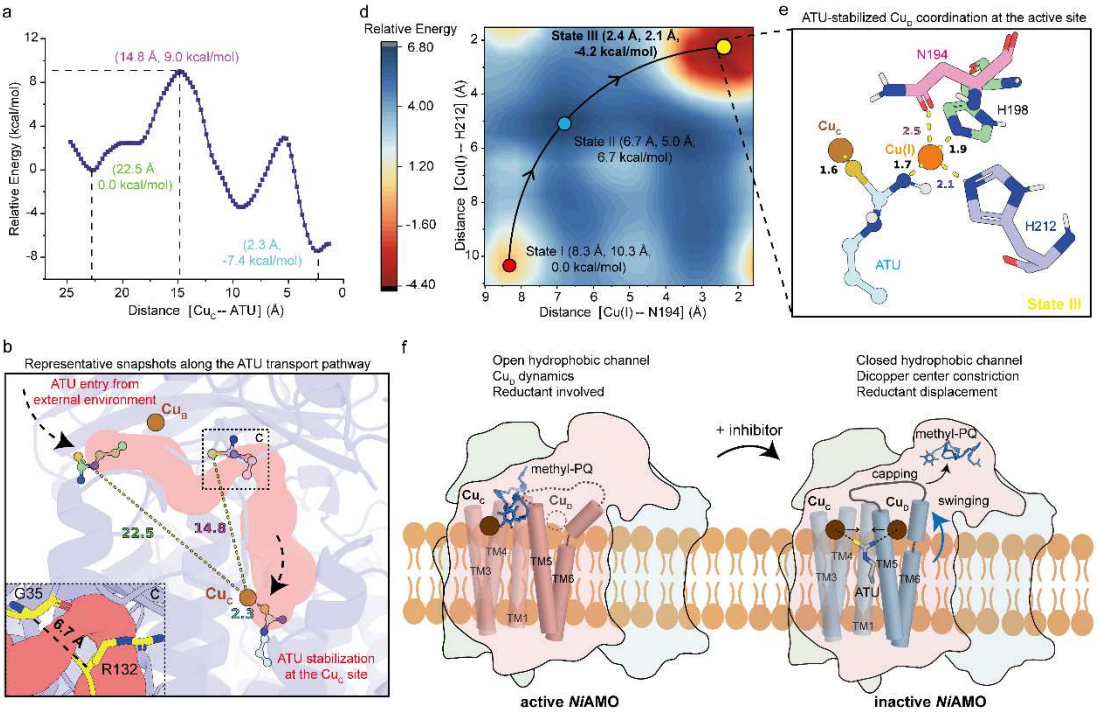


Fig. 4 | ATU-mediated inhibition mechanism on comammox *Ni*AMO. a, US-derived free-energy profile (kcal mol^{-1}) for ATU migration from the extracellular environment into the active site of *Ni*AMO. The reaction coordinate was defined as the distance between the Cu(I) ion at the Cu$_C$ site and the sulfur atom of ATU. **b-c,** Representative conformations of ATU along its migration pathway toward the active site. The representative ATU conformations are displayed as green, pink, and cyan ball-and-stick models, respectively (**b**). The narrowest region of the channel for ATU entry is enlarged in (**c**). The amino acid residues at the narrowest regions are displayed as yellow stick models. **d,** US-derived free-energy landscape (kcal mol^{-1}) for the transition of Cu(I) from the initial non-coordinating configuration (State I) to the Cu$_D$-coordinating configuration (State III). The free-energy landscape was defined by the distances of Cu(I) from N194 and H212. A representative structure illustrating the Cu$_D$-coordinating state and the local coordination geometry of Cu(I) with N194 and H212 is shown in (**e**).

Key interatomic distances are given in Å. **f,** Schematic illustration of ATU-mediated inhibition in comammox *Ni*AMO. In the active state, *Ni*AMO remains an open hydrophobic channel and a quinone-like density is positioned near this Cu_C-Cu_D region. Upon ATU binding, the inhibitor bridges the Cu_C and Cu_D sites, induces rearrangement of the surrounding helices to restrict substrate access. Concurrently, the quinone-like density is displaced from the catalytic center. Copper ions are shown as spheres, and flexible or unresolved regions are indicated by dashed lines.

Multi-omics analysis link *Ni*AMO inhibition to an energy-limited cellular response

To probe cellular responses following direct ATU-mediated *Ni*AMO inhibition, we performed paired transcriptomic-proteomic profiling comparing untreated and ATU-treated *N. inopinata* after 12 h of exposure (Fig. 5). ATU treatment altered both transcript and protein pools, yielding 266 up- and 397 down-regulated transcripts, alongside 177 up- and 59 down-regulated proteins (Fig. 5a). Functional enrichment showed reduced representation of translation, ribosomal biogenesis and energy-production pathways, consistent with a broad downshift in biosynthetic and energy-conservation activity. By contrast, stress-sensing and signal-transduction increased at both transcript and protein levels (Fig. 5b and Supplementary Fig. 22), indicating a non-uniform cellular response rather than a generalized loss of function. Targeted inspection of nitrification-related genes revealed elevated *amoC* transcript abundance under ATU treatment. Together with the direct structural evidence for ATU binding, the absence of coordinated *amo* repression is consistent with inhibition of pre-

462 existing *Ni*AMO rather than transcriptional shutdown of the enzyme complex (Fig. 5c).
463 Several genes encoding respiratory complex I, ATP synthase and NirK were
464 down-regulated, consistent with a broader decrease in energy-conservation and
465 nitrogen-metabolism functions following *Ni*AMO blockade (Fig. 5c). Notably, urease
466 and urea-transport components were up-regulated at both transcriptional and proteomic
467 levels (Fig. 5c). As urea hydrolysis supplies ammonia but does not bypass AMO, we
468 interpret this response as increased substrate-supply capacity compensate for
469 competition under ATU exposure (Fig. 3d). Transcript-protein discordance for cell-
470 division components, including accumulation of FtsB despite repression of cell-cycle
471 transcripts, may reflect different response and turnover timescales and is not taken as
472 evidence for preservation of an active divisome (Fig. 5c).
473 To assess whether differential ATU susceptibility extends to complex environmental
474 communities, we quantified changes in *amoA* gene abundances of AOA, AOB and
475 comammox *Nitrospira* in soil microcosms amended with graded ATU concentrations
476 (Fig. 5d). AOA showed little suppression under the tested conditions, whereas
477 comammox *Nitrospira* displayed greater suppression of net *amoA* gene accumulation
478 than AOB (Fig. 5d), extending the differential ATU response observed in pure culture
479 to this soil microcosm. Collectively, the structural, physiological and multi-omics data
480 link direct *Ni*AMO inhibition to an energy-limited cellular response characterized by
481 reduced biosynthetic functions, stress responses and increased urea-utilization capacity
482 (Fig. 5e).

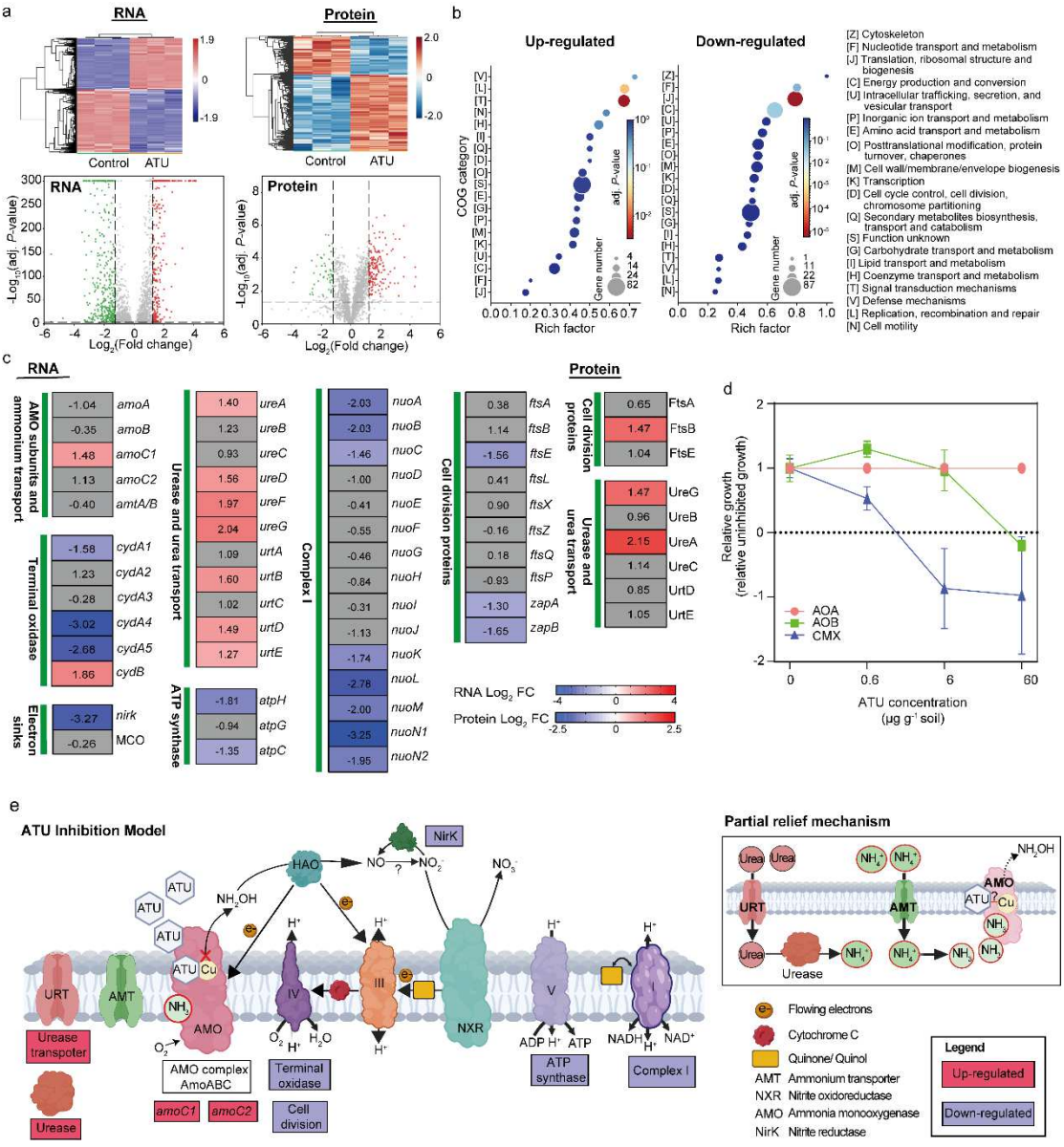


Fig. 5 | Multi-omics insights into ATU-mediated inhibition. a, Transcriptomic and proteomic heatmap of genes and proteins identified as significantly differentially expressed. Volcano plots of differentially expressed genes (DEGs) and proteins (DEPs) in response to ATU treatment. The x-axis shows $\log_2$(fold change) and the y-axis shows -$\log_{10}$(adjusted *P*-value). Thresholds: $|\log_2 FC| > 1.25$ and adjusted $P < 0.001$ for DEGs; $|\log_2 FC| > 1.2$ and adjusted $P < 0.05$ for DEPs. Full genes and proteins significantly changed can be found in Supplementary Data 1. **b,** Enrichment analysis of differentially

expressed genes based on EggNOG database in every cluster from transcriptomic heatmap. **c**, Selected differentially expressed genes and regulated proteins. Full gene and protein annotations can be found in Supplementary Data 2. **d,** Response of soil ammonia oxidizers to ATU treatment. The y-axis shows a relative growth index calculated from *amoA* gene abundance in ATU-treated microcosms relative to untreated controls. A value ≤0 indicates complete inhibition, a value ≥1 indicates no inhibition or potential promotion of growth, and a value between 0 and 1 indicates partial inhibition. n=3 for biologically independent experiments; error bars indicate mean ± SD. **e**, Schematic model of cellular adaptive responses to ATU inhibition. ATU binds and chelates the copper-containing active site of *Ni*AMO, thereby directly blocking the initial ammonia-oxidation reaction and interrupting electron supply for downstream nitrification and respiration. The inset illustrates urea/ammonia-dependent stress-relief strategy. Red boxes mark up-regulated genes/proteins, and purple boxes denote down-regulated components. Key nitrogen-cycling enzymes, transporters and the electron-transport-chain complexes are depicted.

Discussion

Complete nitrification integrates ammonia oxidation and nitrite oxidation within a single cell, yet the structural basis of the catalytic step that initiates this metabolism has remained unresolved. Here, high-resolution structures of inhibitor-free and ATU-bound *Ni*AMO, together with inhibition assays, MD and QM/MM simulations, and multi-omics data support a catalytic and inhibitory architecture that differs from that proposed

for canonical AOB AMO. *Ni*AMO combines a distinct transmembrane architecture, TM6-dominated channel gating and a dynamic, methyl-PQH_2-coupled Cu_D region with pronounced inhibitor susceptibility in *N. inopinata*.

*Ni*AMO contains two auxiliary transmembrane densities that occupy positions distinct from the accessory helices in reported AMO structures from AOB[16,17]. The current cryo-EM maps do not permit unambiguous sequence assignment, but mass spectrometry (Supplementary Fig. 3e) and genomic context[3,41] suggest that these densities may derive from AmoD- or AmoE-like components. Helix1 could alternatively originate from a transmembrane segment associated with putative nitrite oxidoreductase (NXR), which catalyzes the second step of complete nitrification (Supplementary Fig. 3d-e)[3,42]. This possibility raises the testable hypothesis that AMO and NXR are spatially organized within a shared membrane microenvironment, but direct evidence for an AMO-NXR supercomplex, inter-enzyme electron transfer or obligatory substrate channeling will be required.

The most consequential divergence occurs within the Cu_C–Cu_D region. High-resolution AOB AMO structures show the simultaneous occupancy of both Cu_C and Cu_D sites, and have been interpreted in terms of cooperative dicopper mechanism with markedly higher catalytic efficiency than either mononuclear Cu_C or Cu_D alone [15,17,18]. In *Ni*AMO, although both Cu_C and Cu_D are implicated, O_2 activation and substrate oxidation appear to occur predominantly at Cu_D, whereas Cu_C mainly supports local quinone-quinol redox cycling rather than directly participating in the oxygenation chemistry. This functional partitioning supports a Cu_D-centric catalytic pathway that differs from the

concerted dicopper mechanism proposed for AOB AMO [18]. Mechanistically, the two systems appear to diverge after formation of a Cu_D–$OOH^{\bullet-}$ intermediate. In AOB AMO, the relatively close Cu_C–Cu_D geometry permits Cu_D–$OOH^{\bullet-}$ to engage Cu_C and evolve toward a bridging dicopper oxygen species, whereas the larger Cu_C–Cu_D separation and steric constraints in *Ni*AMO favour further HAT and H_2O_2 formation at the mononuclear Cu_D site. Consistently, methyl-PQH_2-mediated formation of the Cu_D(II)–$O^{\bullet-}$ species in *Ni*AMO involves a rate-limiting H_2O_2 activation barrier of 17.5 kcal mol^{-1} (Supplementary Fig. 12), higher than the 14.7 kcal mol^{-1} barrier for the first HAT step that generates the Cu_D(II)–OOH^- intermediate (rate-limiting step) in the $CoQ_{10}H_2$-coupled AOB AMO pathway [18]. Taken together, the distinct fate of the Cu_D(II)–OOH^- intermediate and the resulting higher-barrier mononuclear oxygen-activation pathway may contribute to the substantially lower substrate turnover rate observed in comammox bacteria relative to canonical AOB.

The widened, TM6-regulated channel entrance provides a structural rationale for the high ATU sensitivity of *N. inopinata* relative to the AOB isolate tested here. US indicates that ATU can traverse the channel to the Cu_C region over a free-energy barrier of approximately 9.0 kcal mol^{-1}. Once bound, ATU does more than compete for space: it bridges Cu_C and Cu_D, traps the otherwise dynamic Cu_D coordination environment, orders the E205/F207-containing lid, constricts the channel and displaces the quinone-like density. Thus, the high sensitivity may arise from the combination of accessible inhibitor entry and conformational trapping rather than copper chelation alone. Given the broad distribution of comammox[12], this mechanistic divergence is ecologically

relevant. Sequence analysis shows that key structural elements are highly conserved in comammox clades A and B, including the TM5–TM6 region and Cu_C–Cu_D coordination environment (Fig. 1g), suggesting these structural features may be conserved across the comammox lineage. A broader generalization to comammox requires additional isolates and environmental populations.

The whole-cell rescue assays complement the structural observations by supporting substrate competition between ammonia and ATU for access to the *Ni*AMO catalytic region. Exogenous copper supplementation failed to reverse ATU-mediated ammonia-oxidation suppression, arguing against extracellular copper sequestration and supporting direct inhibition of the intrinsic copper-containing site. Partial relief by excess ammonium or urea-derived ammonia is also consistent with competition for access to *Ni*AMO, a response distinct from that recently reported in AOA[40]. Consistent with this physiological phenotype, multi-omics profiling showed that ATU treatment reduces translation, ribosomal-biogenesis and energy-production functions, consistent with an energy-limited maintenance response, whereas increased stress-signal functions indicate active physiological reprogramming. The concordant increase in urea-transport and urease components is particularly informative: urea hydrolysis cannot bypass *Ni*AMO, but it can increase ammonia supply and thereby provide a plausible compensatory response under competitive ATU inhibition. The soil microcosm data further indicated that, under the tested conditions, comammox *Nitrospira* gene accumulation is more strongly suppressed than that of AOB. These observations connect the atomic-level inhibitory architecture to cellular and

community-level responses, and also imply that urea-driven ammonia supply in soil environments may mitigate ATU inhibition of comammox populations under field conditions.

The *Ni*AMO structure also has practical implications for nitrogen management. AMO controls the entry of fertilizer-derived ammonium into nitrification and thereby influences nitrate formation, nitrogen retention and downstream N_2O production. Comammox contribute to nitrification in agricultural soils[32,34], and *N. inopinata* can grow on guanidine, with comammox-containing soil microcosms indicating that guanidine-derived nitrogen can enter environmental nitrification[14]. Inhibitors developed primarily against AOB may therefore not predictably suppress comammox. The widened *Ni*AMO channel, the Cu_C–Cu_D region and the quinone-access pathway identify three testable determinants for lineage-aware inhibitor design or selection: channel access, copper coordination and disruption of electron/proton delivery. Translation to field application will require validation in soils with quantified comammox activity, together with measurements of nitrogen retention, N_2O emissions and effects on non-target nitrifiers.

Together, these findings show that *Ni*AMO uses a distinct methyl-PQH_2–Cu_D catalytic module and an ATU-responsive gating mechanism, providing a molecular basis for interpreting lineage-specific nitrification in ecosystems and for developing inhibitor strategies that explicitly account for comammox.

Methods

Cultivation of ammonia-oxidizing microorganisms

Three ammonia-oxidizing strains—*Nitrospira inopinata*, *Nitrosopumilus maritimus* SCM1, and *Nitrosomonas halophila* ZJB1—were cultured as previously described[3,4,17]. Briefly, pure cultures of *N. inopinata* were grown in modified AOM medium containing (per liter) KH_2PO_4 (0.05 g), KCl (0.075 g), $MgSO_4 \cdot 7H_2O$ (0.05 g), NaCl (0.58 g), $CaCO_3$ (4 g), together with 1 mL non-chelated trace element solution (TES) and 1 mL selenium-wolfram solution (SWS)[3]. Following autoclaving, the initial pH reached approximately 8.2, and was subsequently maintained near 7.8 during pure-culture growth via the $CaCO_3$-based buffering system[3]. *N. maritimus* SCM1 was cultivated in modified HEPES-buffered synthetic Crenarchaeota medium containing (per liter) NaCl (26 g), $MgSO_4 \cdot 7H_2O$ (5 g), $MgCl_2 \cdot 6H_2O$ (5 g), $CaCl_2 \cdot 2H_2O$ (1.5 g), KBr (0.1 g), 10 mL HEPES buffer (1 mol L^{-1} HEPES with 0.6 mol L^{-1} NaOH, pH 7.5), 5 mL KH_2PO_4 solution (0.4 g L^{-1}), 2 mL bicarbonate solution (1 mol L^{-1}), 1 mL FeNaEDTA solution (7.5 mol L^{-1}), and a mixture containing 1 mL vitamin solution, 1 mL TES, streptomycin (100 mg mL^{-1}), and amphotericin B (1 mg mL^{-1})[4,41,43]. *N. halophila* ZJB1 was maintained in a modified synthetic seawater medium containing (per liter) NaCl (5 g), KCl (0.25 g), $MgSO_4 \cdot 7H_2O$ (0.04 g), $CaCl_2 \cdot 2H_2O$ (0.1 g), 5 mL KH_2PO_4, 1 mL TES and 1 mL phenol red (0.05%) serving as pH indicator. The pH was adjusted to 8.0 using 10% Na_2CO_3[17,44]. Stock cultures were grown in 2 L bottles containing 1.2 L of medium and were supplied with NH_4^+ as the nitrogen source at 3 mmol L^{-1}, 3 mmol L^{-1} and 10 mmol L^{-1} for *N. inopinata*, *N. maritimus* SCM1, and *N. halophila* ZJB1, respectively. *N. inopinata* and *N. maritimus* SCM1 were incubated without agitation at 42 °C and

30 °C, respectively, whereas *N. halophila* ZJB1 was grown with shaking at 120 rpm at 30 °C. To prevent photoinhibition, all strains were kept in darkness. Culture progression was monitored by measuring NH_4^+ consumption and culture purity culture purity was assessed by inoculation into LB broth according to a previously described method[45].

Inhibitor activity assays

The inhibitory responses of AOMs to five commonly used fertilizer additives—allylthiourea (ATU), 3,4-dimethylpyrazole phosphate (DMPP), dicyandiamide (DCD), amidinothiourea (ASU), and nitrapyrin (NP)—were investigated to evaluate the efficacy of NIs against AOMs. For each assay, exponentially growing AOM cells were collected from batch cultures and dispensed into sterile 100 mL glass bottles at 20 mL per bottle, after which the medium was supplemented with the inhibitor of interest across a graded concentration series. Control treatments consisted of identically inoculated cultures lacking NIs. Samples were collected at regular intervals 6 or 12 h to monitor NH_4^+ consumption, thereby tracking AO activity in AOMs.

Chemical analyses

Ammonium was determined using the optimized indophenol blue method[46]. In brief, 200 μL aliquots of culture were transferred into sterile 1.5 mL microcentrifuge tubes and centrifuged at 12,000 rpm for 5 min at room temperature to pellet cellular debris and large particles. The resulting supernatant was transferred to fresh sterile 2 mL Eppendorf tubes and diluted to a final volume of 1 mL with NH_4^+-free ultrapure water. For the optimized indophenol blue method, 50 μL of phenol-nitroprusside solution and 50 μL of alkaline hypochlorite solution were added. Once color development had

reached completion, absorbance was recorded at 630 nm on an EnSpire microplate reader. Final concentrations were calculated using standard curves for NH_4^+ (0-10 μM, $n = 3$, $R^2 > 0.998$).

Membrane fraction extraction and AMO protein purification

For membrane preparation, *N. inopinata* cells were cultured in modified AOM medium either without additive (for active AMO) or in the presence of 10 μM ATU (for inactivated AMO). 80 L of *N. inopinata* cells were harvested by vacuum filtration through a 0.22 μm pore polycarbonate membrane filter (Millipore) and resuspended in 50 mL lysis buffer (50 mM PIPES pH 7.2, 50 mM NaCl, 30 μM $CuSO_4$); for inactivated AMO preparation, the lysis buffer was supplemented with 10 μM ATU throughout. Cell disruption was achieved via ultrasonication (Miou Instrument, Zhejiang, China) at 80% output using a 2 s-on/4 s-off duty cycle over a total of 30 min. The resulting lysate was centrifuged at 12,000 rpm at 4 °C for 30 min to remove cellular debris and intact cells. The supernatant was collected and ultracentrifuged at 150,000 ×g at 4 °C for 2 h. The extracted membrane pellet was resuspended in 100 μL of lysis buffer, then centrifuged at 13,000 rpm and 4 °C for 20 min. The supernatant was discarded, and 100 μL of lysis buffer was added to resuspend the membrane pellet. This washing procedure was repeated three times. Finally, the membrane pellet was resuspended in 40 μL of lysis buffer. Subsequently, n-Decyl-β-D-maltopyranoside (DDM) was added to a final concentration of 0.5%, and the mixture was stirred at 4 °C for 2 h to extract membrane proteins. Afterward, the sample was centrifuged at 13,000 rpm and 4 °C for 10 min to remove cell debris. The supernatant was collected and subjected to ultracentrifugation

at 150,000×g for 2 h at 4 °C to remove ribosomes. The supernatant containing AMO proteins was collected, flash-frozen in liquid nitrogen, and stored at -80 °C until further use.

Preparation of cryo-EM samples and data acquisition

Purified samples were first evaluated by negative-stain electron microscopy on a Talos L120C G2 instrument (Thermo Fisher Scientific) operated at 120 kV. For vitrification, holey-carbon gold grids (Quantifoil R1.2/1.3, 300 mesh) overlaid with a monolayer of graphene (a gift from Jiayue Su, Tsinghua University) were subjected to glow discharge, after which 4 μL of samples was applied onto the front side of the plasma-cleaned grids. Vitrification was accomplished by plunge-freezing into liquid ethane using a Mark IV Vitrobot (ThermoFisher) maintained at 4 °C under 100% relative humidity. Cryo-EM grids were subsequently transferred into liquid nitrogen for storage until data collection. The vitrified samples were loaded into a Titan Krios electron microscope G4 (Thermo Fisher Scientific) operated at 300 kV, equipped with Selectris energy filter (10eV slit width) together with a CEOS CCOR-spherical aberration/chromatic aberration (Cs/Cc) corrector. Automated data collection yielded 15,188 and 8,319 movie stacks for the active and ATU-bound NiAMO datasets, respectively, all recorded on a Falcon 4 detector operated in counting mode at a nominal magnification of ×130,000 (calibrated pixel size of 0.6584 Å). Each movie was dose-fractionated into 40 frames, with a total dose of 50 $^{e-}/Å^2$. Data acquisition was performed using EPU2 software package with a defocus range from -1.2 to -2.0 μm. More data collection details are given in Supplementary Table 4.

Image processing

All raw micrographs were first corrected for beam-induced motion using MotionCor2[47]. The cryoSPARC v4.3.2[48] was used for all downstream image processing. Contrast transfer function (CTF) determination was performed via the Patch CTF routine, and suboptimal micrographs identified by manual inspection were excluded. For particle picking, the Blob Picker was applied using an 8-to-20-nm diameter search window; picked particles were boxed at 224 pixels and Fourier-cropped by a factor of 2. Two-dimensional (2D) classification was then carried out iteratively, and high-quality 2D averages were fed into Topaz[49] for automated particle picking. This two-step procedure—classification followed by Topaz training and re-picking—was cycled four times until 2D class averages ceased to improve. All particles collected across these iterations were pooled, and duplicated entries were eliminated. The resulting non-redundant particle set was used for ab initio volume generation, followed by heterogeneous refinement, which produced several class volumes. The volume exhibiting features of the AMO complex was subsequently refined against prior maps to remove spurious or low-occupancy particles. For the active NiAMO dataset, after three rounds of this reference-based sorting, the best class was re-processed through a fresh ab initio job, then two more heterogeneous refinement steps, and finally subjected to NU refinement with C3 symmetry imposed[50], yielding a 2.47-Å map. For the ATU-treated *Ni*AMO sample, following the same three sorting rounds, the data were directly advanced to NU refinement (C3)[50], which produced a 2.68-Å reconstruction. DeepEMhancer[51] was finally applied to all refined maps to improve density quality for

711 modeling. As a control, the full processing pipeline was also executed without
712 symmetry (C1), which resulted in nearly identical maps with only a marginal loss of
713 resolution.

714 **Model building and refinement**

715 Initial atomic models for NiAmoA, NiAmoB, and NiAmoC were generated de novo
716 using AlphaFold3[52] and rigid-body fitted into the cryo-EM density maps using UCSF
717 Chimera[53]. Subsequent manual model rebuilding was performed in Coot[54], followed by
718 iterative real-space refinement in PHENIX[55] with secondary structure and geometric
719 restraints enforced. The two auxiliary transmembrane helices were modeled as
720 polyalanine due to insufficient side-chain density. Model geometry and map-to-model
721 agreement were evaluated using standard cryo-EM validation metrics. Comprehensive
722 model-building and validation statistics are provided in Supplementary Table 4.

723 **Mass spectrometry analysis**

724 To further characterize the composition of the CMX-AMO complex, the purified AMO
725 samples were resolved on a 4-20% SDS-PAGE gel (Yeasen Biotechnology). The gel
726 bands corresponding to the AMO fractions were then excised and transferred into sterile
727 1.5 mL microcentrifuge tubes. These gel pieces were subsequently washed four times
728 with ultrapure water to remove residual SDS-PAGE running buffer. Finally, the washed
729 AMO protein bands were subjected to LC-MS/MS analysis.

730 Liquid chromatography-tandem mass spectrometry (LC-MS/MS) analysis was
731 performed on a Thermo-Dionex Ultimate 3000 HPLC system coupled to an Orbitrap
732 Fusion mass spectrometer (Thermo Scientific). Peptide separation was achieved over a

120-min gradient at 0.300 μL min^{-1} on a homemade 150-mm C18 column (75 μm i.d.; 5 μm resin; 300 Å). The mobile phase comprised 0.1% formic acid (A) and 0.1% formic acid with 100% acetonitrile (B). Data acquisition was carried out in data-dependent mode via Xcalibur 3.0, with full MS scans collected in the Orbitrap (350-1,550 m/z; 120,000 resolution) followed by 3-s MS/MS scans at 30% normalized collision energy in the ion-routing multipole. The MS/MS spectra were searched against the designated database using Proteome Discoverer (v.1.4).

Copper quantification by inductively coupled plasma mass spectrometry (ICP-MS)

Purified AMO samples were dried in a vacuum centrifugal concentrator (Jiaimu, Beijing, China) and accurately weighed (0.0001 g) portions were transferred into acid-cleaned polytetrafluoroethylene digestion vessels. Samples were pre-digested at room temperature for 30 min with nitric acid and hydrochloric acid (6 ml HNO_3 and 2 ml HCl), then subjected to a stepwise hotplate digestion (100 °C/10 min to 120 °C/10 min to 200 °C/60 min), with acid replenished as needed to prevent drying. After complete digestion, the solution was gently evaporated to ~0.5 mL to remove excess acid, cooled, and made up to 10 mL with metal-free water in a volumetric flask; the vessel was rinsed three times and rinses combined. Copper content was quantified by Agilent 7500CE ICP-MS instrument (Agilent Technologies, USA). The metal content was normalized to the AMO protomer concentration to calculate copper stoichiometry (Supplementary Table 5).

Relief experiments

Following the identification of differentially expressed genes and proteins, 1 L of *N.*

inopinata culture was cultivated and supplemented with 1 mM NH_4^+. After 24 h of incubation, the culture was aliquoted into 20 mL portions in 50 mL sterile plastic centrifuge tubes, and divided into ATU-treated (final concentration 10 μM) and control groups. Following 12 h of ATU exposure, the following reagents were respectively added to assess the recovery capacity from inhibitor-induced stress: $CuCl_2$ (0.5, 5 and 15 μM), NH_4Cl (2 mM), and urea (1 mM). Each condition was performed with three biological replicates. Ammonium concentrations were monitored at 6 h intervals to track the ammonia-oxidizing activity of *N. inopinata*.

Transcriptomic and proteomic analyses

A total of 60 L cultures of *N. inopinata* were grown. Half were maintained as untreated controls, whereas the other half were treated with 10 μM ATU for 12 h. Following treatment, cells from each group were harvested by vacuum filtration onto 0.22-μm pore-size membranes (Millipore), with three biological replicates per condition. The resulting cell pellets were immediately flash-frozen in liquid nitrogen and stored at -80 °C prior to downstream omics analyses.

For transcriptomic profiling, total RNA extracted from growing *N. inopinata* samples was sent to Magigene Biotechnology Co., Ltd. (Guangzhou, China) for cDNA library construction and high-throughput sequencing on an Illumina HiSeq 2500 platform. Differential gene expression between the CMX-control and CMX-ATU (10 μM ATU) groups was evaluated using the DESeq2 R package[56] based on normalized read counts. Transcripts satisfying the criteria of $|\log_2(\text{fold change})| > 1.25$ and adjusted *P*-value < 0.001 were classified as differentially expressed genes (DEGs). Functional annotation

of the assembled unigenes was performed via BLAST searches against the NR database (https://www.ncbi.nlm.nih.gov/). In the R environment, functional enrichment analysis of DEGs was conducted based on the EggNOG database[57].

For quantitative proteomic profiling, an 8-plex iTRAQ reagent kit (AB SCIEX, USA) was applied following a previously described protocol[58] with minor modifications. The iTRAQ-labeled peptide mixtures were initially fractionated by high-pH reversed-phase HPLC on an Agilent 1260 series system fitted with an Agilent 300 Extend C18 column. Peptide separation was then accomplished on an EASY-nLC 1000 UPLC system (ThermoFisher Scientific) equipped with an Acclaim PepMap RSLC reversed-phase analytical column, and tandem mass spectrometry (MS/MS) was acquired on a Q Exactive Hybrid Quadrupole-Orbitrap mass spectrometer (ThermoFisher Scientific). Proteins meeting the thresholds of $|\log_2(\text{fold change})| > 1.20$ and adjusted *P*-value < 0.05 were regarded as differentially expressed proteins (DEPs). Functional annotation and enrichment analyses were performed for the identified proteins. Full details of the transcriptomic and proteomic analyses are available in Supplementary data 1 and 2.

Microcosm incubation

To evaluate the sensitivity of ammonia-oxidizing microorganisms to ATU in agricultural soil, a 30-day soil microcosm incubation experiment was conducted. Surface soil (0-5 cm depth) was collected from M1 site (21.6442°N, 110.9139°E) and subjected to two treatment categories: 100 mg NH_4^+-N kg^{-1} soil + water (control), and 100 mg NH_4^+-N kg^{-1} soil + ATU (0.6, 6 and 60 μg g^{-1} soil). Each treatment was established with three biological replicates. Fresh soil (~20 g, moisture content ~7.0%)

was dispensed into 120 mL serum bottles, and solutions containing ammonium sulfate and ATU were thoroughly mixed with the soil to adjust the water-filled pore space (WFPS) to 50% of maximum water-holding capacity[59]. The bottles were then sealed with black butyl rubber stoppers and incubated at 25 °C in the dark. The stoppers were opened every 3 days for aeration, and the WFPS was maintained at its initial level by weekly addition of ultrapure water. Soil samples were collected on days 0 and 30, immediately frozen in liquid nitrogen and stored at -80°C until DNA extraction.

DNA extraction and quantification of *amoA* gene

Soil DNA was extracted from ~ 0.25 g of the soil using the Soil Genomic DNA Extraction Kit (Tiangen Biotech. Co., Ltd., Beijing, China). The DNA concentrations were measured using the NanoValue™ Plus micronucleic acid analyzer (GE Healthcare Life, Pittsburgh, PA, USA). The extracted DNA was stored at -20 °C for subsequent analyses.

The abundances of AOA, *β*-AOB and comammox clade A were quantified by quantitative PCR (qPCR) targeting archaeal and bacterial *amoA* genes, respectively, using the primers listed in Supplementary Table 6. qPCR reactions were performed on a QuantStudio 5 Real-Time PCR system (Applied Biosystems, CA, USA). Each 20-μL reaction contained 10 μL ChamQ™ Universal SYBR qPCR Master Mix (Vazyme, Nanjing, China), 0.5 μL forward primer, 0.5 μL reverse primer, 1 μL DNA template, and nuclease-free water. All samples and standard reactions were analyzed in triplicate.

Evaluation of ATU efficacy on soil ammonia-oxidizing communities

The inhibitory efficacy of ATU on specific ammonia-oxidizing communities in soil was

evaluated by comparing community growth in inhibitor-amended microcosms relative to that in unamended controls. Relative growth rate was calculated using the following formula:

$$\text{Relative growth} = \frac{NI_x - D_0}{C_x - D_0} \quad (1),$$

where "NI_x" represents gene abundance on day x (day 30) in the presence of the inhibitor, "C_x" represents gene abundance on day x in the control microcosms without any inhibitor, and "D_0" represents gene abundance measured at day 0. If the value of relative growth is ≤ 0, it suggests complete inhibition by the ATU inhibitor; a value ≥ 1 indicates non-inhibition or promotion of growth by the ATU inhibitor; and a value between 0 and 1 indicates partial inhibition.

System setup and molecular dynamics simulations

All molecular dynamics (MD) simulations were performed using the Amber Package, version 22 (University of California, San Francisco, CA)[60]. The initial models of *Ni*AMO determined in this study were employed. For the titratable residues (His, Asp, Glu), protonation state was assigned based on pKa values calculated in the PlayMolecule website (https://open.playmolecule.org)[61] and detailed visual examination of the regional hydrogen-bonded networks. Within the *Ni*AMO monomer, H42 and H44 (in *Ni*AmoA), and H34, H137, H138 and H193 (in *Ni*AmoB) were protonated at the δ position, whereas H23, H172, H215 and H270 (in *Ni*AmoA), H86, H136, H140, H259, H288, H364 and H382 (in *Ni*AmoB), and H43, H127, H140, H198 and H212 (in *Ni*AmoC) were protonated at the ε position. For Asp and Glu residues, D25 (in *Ni*AmoA) was protonated, while the remaining residues were deprotonated.

The membrane environment of *Ni*AMO was constructed using the Packmol-Memgen program[62], with the phospholipid bilayer consisting of 60% phosphatidylvinylethanolamine (PVPE), 20% phosphatidylvinylglycerol (PVPG), and 20% 1-palmitoyl-2-oleoyl-sn-glycero-3-phosphocholine (POPC). The Amber ff14SB[63], Lipid21[64], and GAFF[65] force fields were applied to parameterize the amino acid residues within *Ni*AMO, phospholipid bilayer, and reductants methyl-PQH_2, respectively, while the force field parameters for the Cu_B, Cu_C and Cu_D sites were tailored using the "MCPB.py" tool[66,67] of AmberTools23. The membrane-embedded simulation system was solvated with a periodic rectangular box (the volume is 144.593 × 144.593 × 152.067 $Å^3$) containing 68,853 TIP3P water molecules, 579 lipid molecules, and 0.15 M NaCl.

Following appropriate setup, the complex systems were successively fully minimized by combining 10,000 steps of the steepest-descent method and 10,000 steps of the conjugate gradient method. Then, each system was gradually heated from 0 K to 300 K for a total of 50 ps using the NVT ensemble. To achieve a uniform density after heating dynamics, 1 ns of density equilibrium was executed under the NPT ensemble, during which the temperature and pressure of the system were maintained at 300 K and 1.0 ATM using the Langevin thermostat and the Berendsen barostat[68,69], respectively. Subsequently, all complexes were equilibrated for 2 ns without any restraints in order to relieve minor unfavorable ligand-protein steric interactions that might have been still present. Finally, a production MD simulation of 200 ns was carried out under the NPT ensemble. Throughout the process, the simulation integration step was set to 2 fs, and

the conformational configurations of the complex systems were saved every 100 ps in trajectory files. The covalent bonds connecting hydrogen atoms were then restricted with the SHAKE algorithm[70]. The short-range nonbonded interactions were adopted using a cutoff radius of 8 Å, while the long-range electrostatic interactions were modeled utilizing the Particle mesh Ewald (PME) method with a grid point density of 0.1 nm and an interpolation order of 4[71]. The results of MD simulations were presented by using the Visual Molecular Dynamics version 1.9.3a[72], and PyMOL software was used to exhibit the graphics of the MD simulations.

Umbrella sampling

Umbrella sampling simulations were performed to characterize the free-energy landscapes associated with the Cu ion capture at the Cu_D site and ATU translocation into the active site of *Ni*AMO. Two-dimensional umbrella sampling simulations were conducted for $mPQH_2$-free *Ni*AMO, $mPQH_2$-bound *Ni*AMO, and ATU-bound *Ni*AMO structures to evaluate the thermodynamic feasibility of Cu ion recruitment and stabilization at the Cu_D site. The two-dimensional collective variables were defined as the distances between the Cu ion of Cu_D site and the coordinating residues N194 and H212, respectively. In addition, one-dimensional umbrella sampling simulations were carried out to determine the free-energy profile of ATU translocation from the external solvent environment into the active site of *Ni*AMO, with the reaction coordinate defined as the distance between ATU and the Cu ion at the Cu_C site. Umbrella sampling

windows were generated along each reaction coordinate at 0.2 Å intervals. For each window, 10 ns of MD simulations were performed under a harmonic biasing potential with a force constant of 50 kcal/mol/Å^2. The unbiased potentials of mean force (PMFs) were then reconstructed using the weighted histogram analysis method (WHAM)[73], yielding quantitative free-energy landscapes for Cu ion capture at the Cu_D site and ATU translocation into the *Ni*AMO active site.

QM/MM-MD and metadynamics simulations

All QM/MM Born−Oppenheimer MD simulations were performed utilizing the CP2K program version 2024.1 (https://www.cp2k.org). The initial structures for QM/MM MD simulation were derived from the representative conformations extracted from the classical MD trajectories. The interaction energies of the QM and MM regions were calculated separately using QUICKSTEP[74] and the FIST module within the CP2K program, and the real-space multigrid technique[75] was employed to calculate the electrostatic coupling between the QM and MM regions. The QM region was processed by using a mixed Gaussian and plane wave (GPW) basis set at the DFT (B3LYP) level[76], and the MM region was parametrized in the same way as the classical MD simulation. For the conformational rearrangement of the methyl-PQH$^\bullet$ (mPQH$^\bullet$) radical near the Cu_D site, the QM region comprised the Cu_D(II)–OOH^- species, the side chains of N194, H198, and H212, and the polar headgroup moiety of the mPQH$^\bullet$ radical. For the conformational rearrangement of mPQH$^\bullet$ near the Cu_C site, the QM region included

907 the Cu(I) ion of the Cu_C site, the side chains of D123, H127, H140, protonated D133,
908 and the aromatic ring moiety of the mPQH• radical. All QM atoms at the boundary
909 employed hydrogen-capped atoms to fill the empty valence. The wave function was
910 expanded using a Gaussian double-ζ valence-polarized basis set (DZVP)[77]. An auxiliary
911 plane-wave basis set with a cutoff energy of 360 Ry was implemented to converge the
912 electron density, and combined with the Geodecker−Teter−Hutter (GTH)
913 pseudopotential to handle the core electrons[78]. All QM/MM-MD simulations of 50 ps
914 were performed under the NVT system using 0.5 fs integration steps and the simulated
915 temperature was controlled by canonical sampling through velocity rescaling (CSVR)
916 with a time constant of 10 fs[79].

917 Finally, well-tempered metadynamics simulations[80,81] were performed to characterize
918 the free-energy profiles associated with the conformational rearrangement of the mPQH
919 • radical near the Cu_C and Cu_D sites, respectively. For the mPQH• radical
920 conformational rearrangement near the Cu_D site, the collective variable (CV) was
921 defined as the difference between the two distances connecting the oxygen atoms of the
922 mPQH• radical and the oxygen atom of the Cu_D(II)–OOH^- specie. For the
923 corresponding rearrangement near the Cu_C site, the CV was defined as the difference
924 between the two distances connecting the oxygen atoms of the mPQH• radical and the
925 oxygen atom of protonated D133. Gaussian-shaped potential hills were defined by a
926 width of 0.1 Å, and a height of 0.6 kcal/mol, with a deposition interval of 10 fs.

927

QM/MM calculations

The last snapshot extracted from MD or QM/MM MD trajectories was used for the QM/MM calculations. All QM/MM calculations were performed using ChemShell[82,83], combining turbomole[84] for the QM region and DL_POLY[85] for the MM region. The electrostatic embedding scheme[86] was used to account for the polarizing effect of the protein environment on the QM region. Hydrogen link atoms with the charge-shift model were applied to treat the QM/MM boundary. During QM/MM geometry optimizations, the QM region was studied with the hybrid UB3LYP[87-89] density functional with two levels of theory. For geometry optimization, the double-ζ basis set def2-SVP was used. The energies were further corrected with the larger def2-TZVP basis set for all atoms. Dispersion corrections computed with Grimme's D3 method[90-92] were included in all QM calculations. Candidate transition regions were identified from finely scanned potential-energy surfaces along the specified reaction coordinates using an increment of 0.02 Å, and all minima were optimized without symmetry restraints using the DL-FIND95 optimizer[93]. For the first stage of the H_2O_2 formation, QM/MM calculations were performed for both the open-shell singlet (OSS) and triplet spin states. The QM region was defined to include the polar headgroup moiety of methyl-PQH_2 ($mPQH_2$), the Cu_D(II)–superoxo species, and the directly coordinating residues N194, H198, and H212. For the subsequent generation of the Cu_D(II)–$O^{\bullet-}$ species, the reaction was investigated in the singlet state, with N190 additionally incorporated into the QM region. For the methyl-PQ (mPQ) reduction to $mPQH_2$ near

949 the CuC site, QM/MM calculations were performed to characterize the sequential
950 proton-coupled electron transfer (PCET) processes. The QM region was defined to
951 include the Cu(I) ion at the Cu_C site, the directly coordinating residues D123, H127,
952 and H140, the protonated residue D133, and the polar headgroup moiety of mPQ. The
953 first PCET step was optimized in the open-shell singlet state, while the second PCET
954 step was investigated in the doublet state. The computed relative energies were
955 electronic energies from the QM/MM calculation. The previous work in other
956 metalloenzymes confirmed that the electronic energy barrier is close to the free energy
957 barrier[94-99]. The spin density of QM/MM simulated species are shown in Supplementary
958 Table 3.

959

960 **QM calculations**

961 To evaluate the reaction mechanisms and energetics of the Cu_D site in the oxidation of
962 NH_3 to NH_2OH (Supplementary Fig. 13), density functional theory (DFT) calculations
963 were carried out using the Gaussian 16 software package
964 (https://gaussian.com/citation/). Geometry optimizations were performed at the
965 B3LYP/def2-SVP levels of theory in conjunction with the SMD implicit solvation
966 model[72], followed by single-point energy refinements at the B3LYP/def2-TZVP levels.
967 Given that the *Ni*AMO active site is embedded within the protein–membrane
968 environment, chlorobenzene was selected as the solvent in the SMD model[72] to
969 approximate the hydrophobic milieu. Dispersion corrections computed with Grimme's

D3 method were included in all QM calculations[91,92], with all reported energies further refined using the larger def2-TZVP basis set for all atoms. The energy data are shown in Supplementary Table 2, and the spin density data are shown in Supplementary Table 3.

Data availability

The cryo-EM maps of purified *Ni*AMO complex without (EMD-83338) and with ATU (EMD-83349), have been deposited in the Electron Microscopy Data Bank (http://www.ebi.ac.uk/pdbe/emdb/). The corresponding atomic coordinates (PDB: 45KL and 45LB, respectively) have been deposited in the Protein Data Bank (http://www.rcsb.org), respectively. All other data generated or analyzed during this study are included in this published article and its supplementary information files.

Acknowledgements

We sincerely thank the staff at the cryo-EM center of Southern University of Science and Technology for their technical support on the Cryo-EM and High-Performance Computation platforms. We thank Michael Wagner (University of Vienna, Austria) for helpful discussions. Z.L. is an investigator of SUSTech Institute for Biological Electron Microscopy. This work was supported by the National Natural Science Foundation of China (32570211 to Z.L., 32500022 to X.Y., 22577066 to W.P., and 42573078/42371064 to P.H.) and the Science, Technology and Innovation Commission

of Shenzhen Municipality (JCYJ20240813094922030 to Z.L. and JCYJ20250604144527036 to X.Y.), and Shandong Provincial Natural Science Foundation (ZR2025QB36 to W.P.)

Author Contributions

Z.L., X.Y., W.P. and P.H. supervised the project; T.M. and R.W. carried out cell culture; T.M. carried out membrane extraction and protein purification; T.M. and R.W. performed the biochemical assays; J.Y. and Z.L. prepared the samples for EM and collected the cryo-EM data; X.Y. analyzed cryo-EM data of *Ni*AMO and ATU-treated *Ni*AMO; X.Y., Z.L. and J.Y. performed the model building; J.Y., Z.L. and X.Y. conducted structural analysis; T.M., R.W. and K.L. conducted multi-omics experiments. Z.H. and W.P. designed and performed multiscale computational simulations; J.Y., X.Y., W.P. and Z.L. jointly wrote the initial draft; Z.L. W.P., P.H. and X.Y. edited the manuscript.

Competing Interests Statement: All authors declare no competing interests.

References

1 Kuypers, M. M. M., Marchant, H. K. & Kartal, B. The microbial nitrogen-cycling network. *Nat. Rev. Microbiol.* **16**, 263–276 (2018). https://doi.org/10.1038/nrmicro.2018.9

2 Stein, L. Y. Agritech to Tame the Nitrogen Cycle. *Cold Spring Harb. Perspect. Biol.* **16** (2024). https://doi.org/10.1101/cshperspect.a041668

3 Daims, H. *et al.* Complete nitrification by Nitrospira bacteria. *Nature* **528**, 504–509 (2015). https://doi.org/10.1038/nature16461

4 Könneke, M. *et al.* Isolation of an autotrophic ammonia-oxidizing marine archaeon.

Nature **437**, 543–546 (2005). https://doi.org/10.1038/nature03911

5 Purkhold, U. *et al.* Phylogeny of all recognized species of ammonia oxidizers based on comparative 16S rRNA and amoA sequence analysis: implications for molecular diversity surveys. *Appl. Environ. Microbiol.* **66**, 5368–5382 (2000). https://doi.org/10.1128/aem.66.12.5368-5382.2000

6 van Kessel, M. A. *et al.* Complete nitrification by a single microorganism. *Nature* **528**, 555–559 (2015). https://doi.org/10.1038/nature16459

7 Al-Ajeel, S., Spasov, E., Sauder, L. A., McKnight, M. M. & Neufeld, J. D. Ammonia-oxidizing archaea and complete ammonia-oxidizing Nitrospira in water treatment systems. *Water Res. X* **15**, 100131 (2022). https://doi.org/10.1016/j.wroa.2022.100131

8 Bartelme, R. P., McLellan, S. L. & Newton, R. J. Freshwater Recirculating Aquaculture System Operations Drive Biofilter Bacterial Community Shifts around a Stable Nitrifying Consortium of Ammonia-Oxidizing Archaea and Comammox Nitrospira. *Front. Microbiol.* **8**, 101 (2017). https://doi.org/10.3389/fmicb.2017.00101

9 Fowler, S. J., Palomo, A., Dechesne, A., Mines, P. D. & Smets, B. F. Comammox Nitrospira are abundant ammonia oxidizers in diverse groundwater-fed rapid sand filter communities. *Environ. Microbiol.* **20**, 1002–1015 (2018). https://doi.org/10.1111/1462-2920.14033

10 Jiang, R. *et al.* Salinity changes the nitrification activity and community composition of comammox Nitrospira in intertidal sediments of Yangtze River estuary. *mSystems* **8**, e0102622 (2023). https://doi.org/10.1128/msystems.01026-22

11 Wang, M. *et al.* Newly designed primer pair revealed dominant and diverse comammox amoA gene in full-scale wastewater treatment plants. *Bioresour. Technol.* **270**, 580–587 (2018). https://doi.org/10.1016/j.biortech.2018.09.089

12 Han, P. *et al.* Unveiling unique microbial nitrogen cycling and nitrification driver in coastal Antarctica. *Nat. Commun.* **15**, 3143 (2024). https://doi.org/10.1038/s41467-024-47392-4

13 Kits, K. D. *et al.* Kinetic analysis of a complete nitrifier reveals an oligotrophic lifestyle. *Nature* **549**, 269–272 (2017). https://doi.org/10.1038/nature23679

14 Palatinszky, M. *et al.* Growth of complete ammonia oxidizers on guanidine. *Nature* **633**, 646–653 (2024). https://doi.org/10.1038/s41586-024-07832-z

15 Tucci, F. J. *et al.* Simultaneous occupancy of Cu(C) and Cu(D) in the ammonia monooxygenase active site. *Chem. Sci.* **17**, 4470–4477 (2026). https://doi.org/10.1039/d5sc08447d

16 Tucci, F. J. & Rosenzweig, A. C. Structures of methane and ammonia monooxygenases in native membranes. *Proc. Natl. Acad. Sci. U. S. A.* **122**, e2417993121 (2025). https://doi.org/10.1073/pnas.2417993121

17 Yang, X. *et al.* Structural insights into the catalytic mechanism of ammonia monooxygenase. *Nat. Commun.* **17**, 508 (2025). https://doi.org/10.1038/s41467-025-67194-6

18 Yang, X. *et al.* Structural basis for catalytic and inhibitory divergence between archaeal and bacterial ammonia monooxygenases. *bioRxiv*, 2026.2008.2031.748207 (2026). https://doi.org/10.64898/2026.08.31.748207

19 Chen, Y. *et al.* Ways to mitigate greenhouse gas production from rice cultivation. *J. Environ. Manage.* **368**, 122139 (2024). https://doi.org/10.1016/j.jenvman.2024.122139

20 Ghosh, S. *et al.* Concentration and Isotopic Composition of Atmospheric N2O Over the Last Century. *J. Geophys. Res.: Atmos.* **128**, e2022JD038281 (2023). https://doi.org/10.1029/2022JD038281

21 Prosser, J. I., Hink, L., Gubry-Rangin, C. & Nicol, G. W. Nitrous oxide production by ammonia oxidizers: Physiological diversity, niche differentiation and potential mitigation strategies. *Glob. Chang. Biol.* **26**, 103–118 (2020). https://doi.org/10.1111/gcb.14877

22 Ravishankara, A. R., Daniel, J. S. & Portmann, R. W. Nitrous oxide (N2O): the dominant ozone-depleting substance emitted in the 21st century. *Science* **326**, 123–125 (2009). https://doi.org/10.1126/science.1176985

23 Erisman, J. W. *et al.* Consequences of human modification of the global nitrogen cycle. *Philos. Trans. R. Soc. Lond. B Biol. Sci.* **368**, 20130116 (2013). https://doi.org/10.1098/rstb.2013.0116

24 Kelly, P. T., Taylor, J. M., Andersen, I. M., Stovall, J. & Scott, J. T. Highest primary production achieved at high nitrogen levels despite strong stoichiometric imbalances with phosphorus in hypereutrophic experimental systems. *Limnol. Oceanogr.* **66**, 4375–4390 (2021). https://doi.org/10.1002/lno.11968

25 Martre, P. *et al.* Global needs for nitrogen fertilizer to improve wheat yield under climate change. *Nat. Plants* **10**, 1081–1090 (2024). https://doi.org/10.1038/s41477-024-01739-3

26 Nkebiwe, P. M., Weinmann, M., Bar-Tal, A. & Müller, T. Fertilizer placement to improve crop nutrient acquisition and yield: A review and meta-analysis. *Field Crops Res.* **196**, 389–401 (2016). https://doi.org/10.1016/j.fcr.2016.07.018

27 Abalos, D., Jeffery, S., Sanz-Cobena, A., Guardia, G. & Vallejo, A. Meta-analysis of the effect of urease and nitrification inhibitors on crop productivity and nitrogen use efficiency. *Agric. Ecosyst. Environ.* **189**, 136–144 (2014). https://doi.org/10.1016/j.agee.2014.03.036

28 Beeckman, F., Annetta, L., Corrochano-Monsalve, M., Beeckman, T. & Motte, H. Enhancing agroecosystem nitrogen management: microbial insights for improved nitrification inhibition. *Trends Microbiol.* **32**, 590–601 (2024). https://doi.org/10.1016/j.tim.2023.10.009

29 Shen, T., Stieglmeier, M., Dai, J., Urich, T. & Schleper, C. Responses of the terrestrial ammonia-oxidizing archaeon Ca. Nitrososphaera viennensis and the ammonia-oxidizing bacterium Nitrosospira multiformis to nitrification inhibitors. *FEMS Microbiol. Lett.* **344**, 121–129 (2013). https://doi.org/10.1111/1574-6968.12164

30 Adu-Poku, D., Ackerson, N. O. B., Devine, R. N. O. A. & Addo, A. G. Climate mitigation efficiency of nitrification and urease inhibitors: impact on N2O emission–A review. *Scientific African* **16**, e01170 (2022). https://doi.org/10.1016/j.sciaf.2022.e01170

31 Kösler, J. E., Calvo, O. C., Franzaring, J. & Fangmeier, A. Evaluating the ecotoxicity of nitrification inhibitors using terrestrial and aquatic test organisms. *Environ. Sci. Eur.*

31, 91 (2019). https://doi.org/10.1186/s12302-019-0272-3

32 Li, C., Hu, H.-W., Chen, Q.-L., Chen, D. & He, J.-Z. Growth of comammox Nitrospira is inhibited by nitrification inhibitors in agricultural soils. *J. Soils Sediments* **20**, 621–628 (2020). https://doi.org/10.1007/s11368-019-02442-z

33 Tan, C. Z., Y.; Gubry-Rangin, C.; Yin, C.; Liang, Y. Feasibility and limitations of using specific nitrification inhibitors to differentiate ammonia oxidizer activity. *Soil Biol. Biochem.* **208** (2025). https://doi.org/10.1016/j.soilbio.2025.109848

34 Li, C., Hu, H.-W., Chen, Q.-L., Chen, D. & He, J.-Z. Comammox Nitrospira play an active role in nitrification of agricultural soils amended with nitrogen fertilizers. *Soil Biol. Biochem.* **138**, 107609 (2019). https://doi.org/10.1016/j.soilbio.2019.107609

35 Koo, C. W., Tucci, F. J., He, Y. & Rosenzweig, A. C. Recovery of particulate methane monooxygenase structure and activity in a lipid bilayer. *Science* **375**, 1287–1291 (2022). https://doi.org/10.1126/science.abm3282

36 Tucci, F. J., Jodts, R. J., Hoffman, B. M. & Rosenzweig, A. C. Product analog binding identifies the copper active site of particulate methane monooxygenase. *Nat. Catal.* **6**, 1194–1204 (2023). https://doi.org/10.1038/s41929-023-01051-x

37 Bale, N. J. *et al.* Unusual Plastoquinones in Non-Phototrophic Nitrifying Bacteria. *Environ. Microbiol. Rep.* **17**, e70174 (2025). https://doi.org/10.1111/1758-2229.70174

38 Elling, F. J. *et al.* A novel quinone biosynthetic pathway illuminates the evolution of aerobic metabolism. *Proc. Natl. Acad. Sci. U. S. A.* **122**, e2421994122 (2025). https://doi.org/10.1073/pnas.2421994122

39 Peng, W., Wang, Z., Zhang, Q., Yan, S. & Wang, B. Unraveling the Valence State and Reactivity of Copper Centers in Membrane-Bound Particulate Methane Monooxygenase. *J. Am. Chem. Soc.* **145**, 25304–25317 (2023). https://doi.org/10.1021/jacs.3c08834

40 Dalkidis, D. *et al.* Common nitrification inhibitors exhibit varied physiological mechanisms on an ammonia-oxidizing microorganism. *bioRxiv*, 2026.2005.2010.724060 (2026). https://doi.org/10.64898/2026.05.10.724060

41 Palatinszky, M. *et al.* Cyanate as an energy source for nitrifiers. *Nature* **524**, 105–108 (2015). https://doi.org/10.1038/nature14856

42 Chicano, T. M. *et al.* Structural and functional characterization of the intracellular filament-forming nitrite oxidoreductase multiprotein complex. *Nat. Microbiol.* **6**, 1129–1139 (2021). https://doi.org/10.1038/s41564-021-00934-8

43 Qin, W. *et al.* Nitrosopumilus maritimus gen. nov., sp. nov., Nitrosopumilus cobalaminigenes sp. nov., Nitrosopumilus oxyclinae sp. nov., and Nitrosopumilus ureiphilus sp. nov., four marine ammonia-oxidizing archaea of the phylum Thaumarchaeota. *Int. J. Syst. Evol. Microbiol.* **67**, 5067–5079 (2017). https://doi.org/10.1099/ijsem.0.002416

44 Bollmann, A., French, E. & Laanbroek, H. J. Isolation, cultivation, and characterization of ammonia-oxidizing bacteria and archaea adapted to low ammonium concentrations. *Methods Enzymol.* **486**, 55–88 (2011). https://doi.org/10.1016/b978-0-12-381294-0.00003-1

45 Qin, W. *et al.* Marine ammonia-oxidizing archaeal isolates display obligate mixotrophy

and wide ecotypic variation. *Proc. Natl. Acad. Sci. U. S. A.* **111**, 12504–12509 (2014). https://doi.org/10.1073/pnas.1324115111

46 Mantoura, R. F. C. W., E.M.S. Optimization of the indophenol blue method for the automated determination of ammonia in estuarine waters. *Estuar. Coast. Shelf Sci.* **17**, 6 (1983). https://doi.org/10.1016/0272-7714(83)90067-7

47 Zheng, S. Q. *et al.* MotionCor2: anisotropic correction of beam-induced motion for improved cryo-electron microscopy. *Nat. Methods* **14**, 331–332 (2017). https://doi.org/10.1038/nmeth.4193

48 Punjani, A., Rubinstein, J. L., Fleet, D. J. & Brubaker, M. A. cryoSPARC: algorithms for rapid unsupervised cryo-EM structure determination. *Nat. Methods* **14**, 290–296 (2017). https://doi.org/10.1038/nmeth.4169

49 Bepler, T. *et al.* Positive-unlabeled convolutional neural networks for particle picking in cryo-electron micrographs. *Nat. Methods* **16**, 1153–1160 (2019). https://doi.org/10.1038/s41592-019-0575-8

50 Punjani, A., Zhang, H. & Fleet, D. J. Non-uniform refinement: adaptive regularization improves single-particle cryo-EM reconstruction. *Nat. Methods* **17**, 1214–1221 (2020). https://doi.org/10.1038/s41592-020-00990-8

51 Sanchez-Garcia, R. *et al.* DeepEMhancer: a deep learning solution for cryo-EM volume post-processing. *Commun. Biol.* **4**, 874 (2021). https://doi.org/10.1038/s42003-021-02399-1

52 Abramson, J. *et al.* Accurate structure prediction of biomolecular interactions with AlphaFold 3. *Nature* **630**, 493–500 (2024). https://doi.org/10.1038/s41586-024-07487-w

53 Pettersen, E. F. *et al.* UCSF Chimera--a visualization system for exploratory research and analysis. *J. Comput. Chem.* **25**, 1605–1612 (2004). https://doi.org/10.1002/jcc.20084

54 Emsley, P. & Cowtan, K. Coot: model-building tools for molecular graphics. *Acta Crystallogr. D Biol. Crystallogr.* **60**, 2126–2132 (2004). https://doi.org/10.1107/s0907444904019158

55 Adams, P. D. *et al.* PHENIX: a comprehensive Python-based system for macromolecular structure solution. *Acta Crystallogr. D Biol. Crystallogr.* **66**, 213–221 (2010). https://doi.org/10.1107/s0907444909052925

56 Love, M. I., Huber, W. & Anders, S. Moderated estimation of fold change and dispersion for RNA-seq data with DESeq2. *Genome Biol.* **15**, 550 (2014). https://doi.org/10.1186/s13059-014-0550-8

57 Huerta-Cepas, J. *et al.* eggNOG 5.0: a hierarchical, functionally and phylogenetically annotated orthology resource based on 5090 organisms and 2502 viruses. *Nucleic Acids Res.* **47**, D309–D314 (2019). https://doi.org/10.1093/nar/gky1085

58 Zhao, H. M. *et al.* Global Picture of Protein Regulation in Response to Dibutyl Phthalate (DBP) Stress of Two Brassica parachinensis Cultivars Differing in DBP Accumulation. *J. Agric. Food. Chem.* **66**, 4768–4779 (2018). https://doi.org/10.1021/acs.jafc.8b01157

59 Xia, W. *et al.* Autotrophic growth of nitrifying community in an agricultural soil. *ISME*

J. **5**, 1226–1236 (2011). https://doi.org/10.1038/ismej.2011.5

60 Lee, T. S. *et al.* Alchemical Binding Free Energy Calculations in AMBER20: Advances and Best Practices for Drug Discovery. *J. Chem. Inf. Model.* **60**, 5595–5623 (2020). https://doi.org/10.1021/acs.jcim.0c00613

61 Torrens-Fontanals, M., Tourlas, P., Doerr, S. & De Fabritiis, G. PlayMolecule Viewer: A Toolkit for the Visualization of Molecules and Other Data. *J. Chem. Inf. Model.* **64**, 584–589 (2024). https://doi.org/10.1021/acs.jcim.3c01776

62 Schott-Verdugo, S. & Gohlke, H. PACKMOL-Memgen: A Simple-To-Use, Generalized Workflow for Membrane-Protein-Lipid-Bilayer System Building. *J. Chem. Inf. Model.* **59**, 2522–2528 (2019). https://doi.org/10.1021/acs.jcim.9b00269

63 Maier, J. A. *et al.* ff14SB: Improving the Accuracy of Protein Side Chain and Backbone Parameters from ff99SB. *J. Chem. Theory Comput.* **11**, 3696–3713 (2015). https://doi.org/10.1021/acs.jctc.5b00255

64 Dickson, C. J., Walker, R. C. & Gould, I. R. Lipid21: Complex Lipid Membrane Simulations with AMBER. *J. Chem. Theory Comput.* **18**, 1726–1736 (2022). https://doi.org/10.1021/acs.jctc.1c01217

65 Wang, J., Wolf, R. M., Caldwell, J. W., Kollman, P. A. & Case, D. A. Development and testing of a general amber force field. *J. Comput. Chem.* **25**, 1157–1174 (2004). https://doi.org/10.1002/jcc.20035

66 Li, P. & Merz, K. M., Jr. MCPB.py: A Python Based Metal Center Parameter Builder. *J. Chem. Inf. Model.* **56**, 599–604 (2016). https://doi.org/10.1021/acs.jcim.5b00674

67 Li, P. & Merz, K. M., Jr. Metal Ion Modeling Using Classical Mechanics. *Chem. Rev.* **117**, 1564–1686 (2017). https://doi.org/10.1021/acs.chemrev.6b00440

68 Doshi, U. & Hamelberg, D. Extracting Realistic Kinetics of Rare Activated Processes from Accelerated Molecular Dynamics Using Kramers' Theory. *J. Chem. Theory Comput* **7**, 575–581 (2011). https://doi.org/10.1021/ct1005399

69 Lin, Y., Pan, D., Li, J., Zhang, L. & Shao, X. Application of Berendsen barostat in dissipative particle dynamics for nonequilibrium dynamic simulation. *J. Chem. Phys.* **146**, 124108 (2017). https://doi.org/10.1063/1.4978807

70 Kräutler, V., van Gunsteren, W. F. & Hünenberger, P. H. A fast SHAKE algorithm to solve distance constraint equations for small molecules in molecular dynamics simulations. *J. Comput. Chem.* **22**, 501–508 (2001). https://doi.org/10.1002/1096-987X(20010415)22:5<501::AID-JCC1021>3.0.CO;2-V

71 Simmonett, A. C. & Brooks, B. R. A compression strategy for particle mesh Ewald theory. *J. Chem. Phys.* **154**, 054112 (2021). https://doi.org/10.1063/5.0040966

72 Marenich, A. V., Cramer, C. J. & Truhlar, D. G. Universal solvation model based on solute electron density and on a continuum model of the solvent defined by the bulk dielectric constant and atomic surface tensions. *J. Phys. Chem. B* **113**, 6378–6396 (2009). https://doi.org/10.1021/jp810292n

73 Kästner, J. Umbrella sampling. *WIREs Comput. Mol. Sci.* **1**, 932–942 (2011). https://doi.org/10.1002/wcms.66

74 VandeVondele, J. *et al.* Quickstep: Fast and accurate density functional calculations using a mixed Gaussian and plane waves approach. *Comput. Phys. Commun.* **167**, 103–

128 (2005). https://doi.org/10.1016/j.cpc.2004.12.014

75 Martí, S., Moliner, V. & Tuñón, I. Improving the QM/MM Description of Chemical Processes: A Dual Level Strategy To Explore the Potential Energy Surface in Very Large Systems. [J. Chem. Theory Comput. 1, 1008-1016 (2005)]. *J. Chem. Theory Comput.* **2**, 216 (2006). https://doi.org/10.1021/ct058001a

76 Sun, Q., Berkelbach, T. C., McClain, J. D. & Chan, G. K. Gaussian and plane-wave mixed density fitting for periodic systems. *J. Chem. Phys.* **147**, 164119 (2017). https://doi.org/10.1063/1.4998644

77 VandeVondele, J. & Hutter, J. Gaussian basis sets for accurate calculations on molecular systems in gas and condensed phases. *J. Chem. Phys.* **127**, 114105 (2007). https://doi.org/10.1063/1.2770708

78 Krack, M. Pseudopotentials for H to Kr optimized for gradient-corrected exchange-correlation functionals. *Theor. Chem. Acc.* **114**, 145–152 (2005). https://doi.org/10.1007/s00214-005-0655-y

79 Bussi, G., Donadio, D. & Parrinello, M. Canonical sampling through velocity rescaling. *J Chem Phys* **126**, 014101 (2007). https://doi.org/10.1063/1.2408420

80 Barducci, A., Bonomi, M. & Parrinello, M. Metadynamics. *WIREs Comput. Mol. Sci.* **1**, 826–843 (2011). https://doi.org/10.1002/wcms.31

81 Laio, A. & Gervasio, F. L. Metadynamics: a method to simulate rare events and reconstruct the free energy in biophysics, chemistry and material science. *Rep. Prog. Phys.* **71**, 126601 (2008). https://doi.org/10.1088/0034-4885/71/12/126601

82 de Vries, A. H. *et al.* Zeolite Structure and Reactivity by Combined Quantum-Chemical−Classical Calculations. *J. Phys. Chem. B* **103**, 6133–6141 (1999). https://doi.org/10.1021/jp9913012

83 Metz, S., Kästner, J., Sokol, A. A., Keal, T. W. & Sherwood, P. ChemShell—a modular software package for QM/MM simulations. *WIREs Comput. Mol. Sci.* **4**, 101–110 (2014). https://doi.org/10.1002/wcms.1163

84 Furche, F. *et al.* Turbomole. *WIREs Comput. Mol. Sci.* **4**, 91–100 (2014). https://doi.org/10.1002/wcms.1162

85 Smith, W., Yong, C. W. & Rodger, P. M. DL_POLY: Application to molecular simulation. *Mol. Simul.* **28**, 385–471 (2002). https://doi.org/10.1080/08927020290018769

86 Bakowies, D. & Thiel, W. Hybrid Models for Combined Quantum Mechanical and Molecular Mechanical Approaches. *J. Phys. Chem.* **100**, 10580–10594 (1996). https://doi.org/10.1021/jp9536514

87 Dandu, N. K., Adeyiga, O., Panthi, D., Bird, S. A. & Odoh, S. O. Performance of density functional theory for describing hetero-metallic active-site motifs for methane-to-methanol conversion in metal-exchanged zeolites. *J. Comput. Chem.* **39**, 2667–2678 (2018). https://doi.org/10.1002/jcc.25714

88 Dandu, N. K., Reed, J. A. & Odoh, S. O. Performance of Density Functional Theory for Predicting Methane-to-Methanol Conversion by a Tri-Copper Complex. *J. Phys. Chem. C* **122**, 1024–1036 (2017). https://doi.org/10.1021/acs.jpcc.7b09284

89 Yu, H. S., He, X., Li, S. L. & Truhlar, D. G. Correction: MN15: A Kohn-Sham global-

hybrid exchange-correlation density functional with broad accuracy for multi-reference and single-reference systems and noncovalent interactions. *Chem. Sci.* **7**, 6278–6279 (2016). https://doi.org/10.1039/c6sc90044e

90 Grimme, S. Semiempirical GGA-type density functional constructed with a long-range dispersion correction. *J. Comput. Chem.* **27**, 1787–1799 (2006). https://doi.org/10.1002/jcc.20495

91 Grimme, S., Antony, J., Ehrlich, S. & Krieg, H. A consistent and accurate ab initio parametrization of density functional dispersion correction (DFT-D) for the 94 elements H-Pu. *J. Chem. Phys.* **132**, 154104 (2010). https://doi.org/10.1063/1.3382344

92 Grimme, S., Ehrlich, S. & Goerigk, L. Effect of the damping function in dispersion corrected density functional theory. *J. Comput. Chem.* **32**, 1456–1465 (2011). https://doi.org/10.1002/jcc.21759

93 Kästner, J. *et al.* DL-FIND: an open-source geometry optimizer for atomistic simulations. *J. Phys. Chem. A* **113**, 11856–11865 (2009). https://doi.org/10.1021/jp9028968

94 Hu, Y. *et al.* Reprogramming of Phenylalanine Dehydrogenase Enables Synthesis of N-Alkyl-α-amino Acids. *ACS Catalysis* **16**, 9760–9766 (2026). https://doi.org/10.1021/acscatal.6c02211

95 Li, H. & Liu, Y. Mechanistic Investigation of Isonitrile Formation Catalyzed by the Nonheme Iron/α-KG-Dependent Decarboxylase (ScoE). *ACS Catalysis* **10**, 2942–2957 (2020). https://doi.org/10.1021/acscatal.9b05411

96 Senn, H. M., Thiel, S. & Thiel, W. Enzymatic Hydroxylation in p-Hydroxybenzoate Hydroxylase: A Case Study for QM/MM Molecular Dynamics. *J. Chem. Theory Comput.* **1**, 494–505 (2005). https://doi.org/10.1021/ct049844p

97 Shaik, S. *et al.* P450 enzymes: their structure, reactivity, and selectivity-modeled by QM/MM calculations. *Chem. Rev.* **110**, 949–1017 (2010). https://doi.org/10.1021/cr900121s

98 Zhang, Y., Liu, H. & Yang, W. Free energy calculation on enzyme reactions with an efficient iterative procedure to determine minimum energy paths on a combined ab initio QM/MM potential energy surface. *J. Chem. Phys.* **112**, 3483–3492 (2000). https://doi.org/10.1063/1.480503

99 Zhao, C., Li, Y., Wang, C. & Chen, H. Mechanistic Dichotomy in the Activation of SAM by Radical SAM Enzymes: QM/MM Modeling Deciphers the Determinant. *ACS Catalysis* **10**, 13245–13250 (2020). https://doi.org/10.1021/acscatal.0c03384

Supplementary Files

This is a list of supplementary files associated with this preprint. Click to download.

- SICMX20261016.pdf